Climate Dynamics (2026) 64:315
https://doi.org/10.1007/s00382-026-08205-0

ORIGINAL ARTICLE

Regional nudged storylines for the European hot and dry summers 2018–2022: response of evapotranspiration regimes to climate change

Tatiana Klimiuk[1] · Antonio Sanchez-Benitez[2] · Patrick Ludwig[1] · Joaquim G. Pinto[1]

Received: 9 October 2025 / Accepted: 19 April 2026

Abstract
Europe has recently experienced a series of hot and dry summers. Previous case studies indicate that, for a given atmospheric circulation, heatwave temperatures may increase by 1.5–3 K per degree of global warming, but the magnitude of this amplification varies substantially across regions and events, and its underlying mechanisms remain insufficiently constrained. Here, we investigate this variability using circulation-nudged regional climate storylines for the summers 2018–2022, dynamically downscaled over Europe and spanning climates from pre-industrial conditions to +4 K global warming. The present-day simulations realistically reproduce observed temperature, soil moisture, and surface fluxes. We find that warming amplification is spatially heterogeneous and seasonally dependent, with the strongest amplification over Central Europe occurring in August, indicating a disproportionate intensification of late-summer heatwaves. Using the evaporative fraction-soil moisture framework, we show that warming amplification is closely linked to changes in the evapotranspiration regime. The strongest amplification occurs when warming induces a transition from energy-limited to moisture-limited conditions, triggering rapid soil moisture depletion, a pronounced reduction in evaporative fraction, and enhanced sensible heating. In contrast, amplification is weaker when conditions are already moisture-limited in the pre-industrial climate, due to the reduced potential for further soil drying, and weakest when the regime remains energy-limited. These findings demonstrate that spatial and event-to-event differences in warming amplification can partially be attributed to the sensitivity of land-atmosphere coupling to soil moisture changes. Accounting for these feedbacks is essential for robust projections of future heat extremes and for identifying regions most vulnerable to disproportionate increases in heatwave intensity.

Keywords Regional climate modeling · Land-atmosphere coupling · Heatwave · Storyline approach

1 Introduction

Extreme heat events in Europe have become more frequent and intense in recent years - a trend expected to persist as global temperatures continue to rise (Meehl and Tebaldi 2004; Fischer and Schär 2010; Perkins et al. 2012; Seneviratne et al. 2021). The period 2018–2022 is especially marked in the literature as a multi-year series of heatwaves and droughts over Central Europe (Rakovec et al. 2022; Knutzen et al. 2025). It started in 2018 with a precipitation-deprived anomalously hot summer (Dirmeyer et al. 2021; Rousi et al. 2023; Aalbers et al. 2023), continued with a sequence of two unprecedented heatwaves in June and July 2019 (Sousa et al. 2020; Vries et al. 2024; Klimiuk et al. 2025), and culminated in 2022 with a prolonged compound heatwave-drought event (Tripathy and Mishra 2023; Bevacqua et al. 2024; Feser et al. 2024). Extreme heat events are typically associated with persistent large-scale circulation anomalies, such as atmospheric blocking or subtropical ridges (Sousa et al. 2018, 2021; Kautz et al. 2022; Barriopedro et al. 2023). Furthermore, the intensity of such events is strongly influenced by antecedent and concurrent soil conditions (Fischer et al. 2007; Miralles et al. 2019; Sousa et al. 2020). Land-atmosphere feedbacks, particularly the coupling between soil moisture and evapotranspiration,

✉ Tatiana Klimiuk
tatiana.klimiuk@kit.edu

[1] Institute of Meteorology and Climate Research - Troposphere Research (IMKTRO), Karlsruhe Institute of Technology (KIT), Karlsruhe, Germany

[2] Alfred Wegener Institute, Helmholtz-Centre for Polar and Marine Research, Bremerhaven, Germany

play a crucial role in modulating the temperature variability (Seneviratne et al. 2010; Miralles et al. 2014, 2019; Lemus-Canovas et al. 2025).

Consequently, the expected intensification of heatwaves may result from both changes in large-scale circulation and the thermodynamic effects of climate warming. However, projections of future changes in the characteristics of large-scale weather systems remain uncertain, due to internal variability and model limitations (Kautz et al. 2022). Recent synthesis studies further highlight either a lack of significant change or substantial disagreement among models regarding future atmospheric circulation over Europe (Schaller et al. 2018; Huguenin et al. 2020; Woollings et al. 2025).

To address the challenge of disentangling thermodynamic and dynamic effects of climate warming, various storyline approaches have emerged in recent years (Shepherd et al. 2018; Baulenas et al. 2023; Baldissera Pacchetti et al. 2024). One such approach is the construction of event-based storylines, which place present-day circulation patterns into different counterfactual climates by means of spectral nudging of large-scale circulation (Wehrli et al. 2020; Garderen et al. 2021; Sánchez-Benítez et al. 2022; Feser and Shepherd 2025). Previous studies, such as Sánchez-Benítez et al. (2022); Klimiuk et al. (2025), and Zhuo et al. (2025), have demonstrated that the response of near-surface temperatures to global warming is highly event-specific and spatially variable. For instance, the maximum 2 m-temperature response during the July 2019 European heatwave exceeded 3 KK^{-1} on some days, translating to a 12 K increase in maximum temperatures in a +4 K warmer world compared to pre-industrial conditions. The case study by Klimiuk et al. (2025) also highlighted an increase in the diurnal variability, with daily maximum temperatures in July and August exhibiting a stronger response of maximum temperatures than that of minimum temperatures.

An important advantage of the nudged storyline approach is that, with the large-scale circulation constrained to follow the present-day evolution across all global warming levels (GWLs), it allows the thermodynamic response to be isolated and the variation of local increments with GWL to be assessed at each grid point on a daily timescale. This cannot be achieved with free-running models. On the other hand, the possible influence of local interactions on the global circulation is not represented in nudged storylines. Thus, both approaches provide valuable insights into different components of climate change.

Surface- and root-zone soil moisture is a fundamental control on summertime temperatures through its coupling with evapotranspiration (Seneviratne et al. 2010; Zeppetello et al. 2019; Miralles et al. 2019; Dong et al. 2022; Lemus-Canovas et al. 2025). However, in the case of humid soil conditions, evapotranspiration is largely independent of soil moisture and primarily controlled by incoming radiation. This case is known as an energy-limited evapotranspiration (soil moisture) regime (Seneviratne et al. 2010; Feldman et al. 2019; Fu et al. 2024). When soil moisture falls below a critical threshold (θ_{crit}), evapotranspiration decreases with declining soil moisture, becoming limited by soil water availability (Seneviratne et al. 2010; Schwingshackl et al. 2017) - thus evapotranspiration enters a moisture-limited regime. The associated reduction in evaporative cooling leads to an increase in sensible heat flux and thus an increase in daily maximum near-surface temperatures (Seneviratne et al. 2010; Fu et al. 2024).

The increased sensitivity of evapotranspiration to soil moisture in the moisture-limited regime is reflected by a stronger positive temporal correlation $\rho(\lambda E, \theta)$ between latent heat flux λE and soil moisture θ, where λ stands for latent heat of vaporization of water, and E is evaporation rate (e.g., Santanello et al. 2018; Rousi et al. 2023). The reduced evaporative cooling typically manifests itself in a negative correlation between the latent heat flux λE and near-surface temperature T under moisture-limited conditions ($\rho(\lambda E, T)$, e.g., Seneviratne et al. 2010; Gevaert et al. 2018). Both mechanisms – the suppression of evapotranspiration due to soil moisture limitations and the associated amplification of near-surface temperatures – constitute fundamental aspects underlying the soil moisture-temperature coupling, and the magnitudes of the respective correlations reflect the strength of this coupling (e.g., Seneviratne et al. 2010).

A widely used conceptual framework describing the relationship between soil moisture and evapotranspiration was first introduced by Budyko et al. (1980) and has been applied extensively ever since, as it adequately approximates the observed and modeled behavior of evapotranspiration (e.g., Koster et al. 2009; Seneviratne et al. 2010; Schwingshackl et al. 2017, 2018; Zeppetello et al. 2019; Koster et al. 2024). According to this framework, the evaporative fraction $EF = \frac{\lambda E}{R_n}$, defined as the ratio of latent heat flux λE to net radiation R_n at the surface, exhibits a linear dependency on soil moisture in the moisture-limited regime. Above the critical soil moisture threshold (i.e., in the energy-limited regime), EF remains approximately constant (see Fig. 1).

Nevertheless, the conceptual framework shown in Fig. 1 is an approximation of a complex system, and the transition between energy-limited and moisture-limited regimes is often better described as a continuous, nonlinear response emerging from land-atmosphere feedbacks than a distinct regime shift. For example, Zeppetello et al. (2019) showed that the dependence of evaporation on soil moisture, which is empirically described by the introduction of moisture- and energy-limited regimes, relies on a fundamental feature of land-atmosphere interactions: a counteraction between the

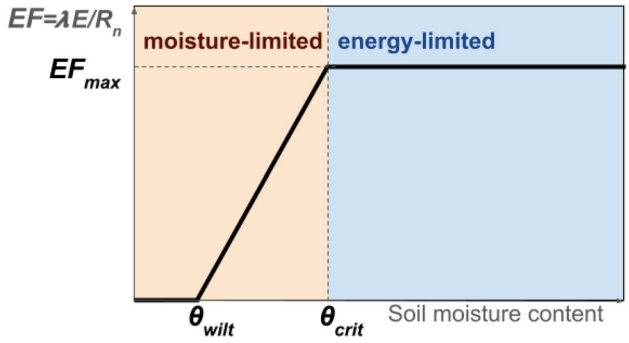

Fig. 1 Conceptual framework describing the dependency of evaporative fraction (EF) on soil moisture, adapted from Seneviratne et al. (2010), their Fig. 5. θ_{wilt} is wilting point; θ_{crit} is critical soil moisture, EF_{max} is maximal reachable evaporative fraction, and R_n is net radiation flux at surface

evaporative cooling and the vapor pressure deficit governed by the Clausius-Clapeyron relationship. The actual shape of the EF(θ) relationship (namely the value of the apparent critical soil moisture θ_{crit}, the slope of the dry part of the relationship and the maximum evapotranspiration) is multidimensional, with the dependency on radiative conditions and atmospheric demand, as well as plant physiology and soil properties (Haghighi et al. 2018; Feldman et al. 2019; Peng et al. 2019). In this context, Benson and Dirmeyer (2021) distinguish weakly coupled, sensitive, and hypersensitive soil-moisture regimes based on the diagnosed sensitivity of near-surface air temperature and turbulent heat fluxes to soil moisture, identifying a soil-moisture breakpoint separating the sensitive and hypersensitive regimes. Thus, θ_{crit} should not be interpreted as a universal physical threshold, but rather as a state-dependent, emergent diagnostic that summarizes the dominant land-atmosphere coupling behavior under a given set of environmental and climatic conditions. While point-level $EF(\theta)$ relationships exhibit substantial scatter, the resulting θ_{crit} can remain statistically robust when estimated over sufficiently large samples or multi-year periods, reflecting the relative stationarity of the underlying climatic and land-surface controls (Schwingshackl et al. 2017; Benson and Dirmeyer 2021; Hsu et al. 2024).

In response to global warming, the occurrence of the moisture-limited evapotranspiration regime may increase in summer, leading to the intensification of extreme heat events. Using event-based storyline simulations with prescribed large-scale atmospheric circulation, we provide a framework to estimate shifts in soil moisture regimes and their influence on temperature responses during specific heatwaves. In particular, a shift toward the moisture-limited regime can strengthen soil moisture-temperature coupling, leading to amplified heatwave intensity under otherwise similar circulation conditions.

In this paper, we investigate the properties and responses of heatwaves that occurred during the series of hot and dry summers between 2018 and 2022 in Europe (Knutzen et al. 2025) using regional nudged storylines (Klimiuk et al. 2025). The objective of this study is to estimate the role of the soil moisture-temperature coupling in modulating the response of maximum temperatures to global warming. Understanding land-atmosphere feedbacks is crucial, as areas not previously considered heatwave hotspots may become increasingly susceptible to extreme temperatures, necessitating proactive adaptation measures.

More specifically, the following research questions are addressed:

1. How well do the model simulations capture the land-atmosphere conditions during 2018–2022?
2. What are the characteristics of the near-surface temperature response to global warming?
3. How does the evapotranspiration regime respond to climate change in the nudged regional storyline simulations?
4. Is there a connection between the evapotranspiration regime change and the magnitude of the near-surface temperature response?

The paper is structured as follows. Section 2 provides a detailed description of the data and methods used in this study. In Sect. 3.1, we provide an overview of the studied period and present the model evaluation results. Section 3.2 explores the temperature response to global warming, specifically examining how the temperature response depends on the present-day temperature values and how it varies throughout the summer season. Section 3.3 examines the response of evapotranspiration regimes based on the $EF(\theta)$ framework, evaluating how the soil moisture-evapotranspiration relationship evolves under different warming scenarios. In Sect. 3.4, the potential connection between the evapotranspiration regime change and the magnitude of the temperature response is examined. Finally, Sect. 4 discusses the findings and summarizes the final conclusions.

2 Data and methods

2.1 Nudged storyline simulations

In this study, we use regional climate storylines for the period 2017–2022, extensively described in Klimiuk et al. (2025). For completeness, we summarize the essential details below.

The regional simulations are driven by global storylines based on the coupled climate model AWI-CM−1.1-MR (AWI-CM1; Semmler et al. 2020). In the global storylines,

the atmospheric circulation is constrained by spectral nudging of vorticity and divergence toward ERA5 reanalysis (Hersbach et al. 2020) between 700–100 hPa and for zonal wavenumbers $\leq$20, using a 24 h e-folding time. This ensures that only the large-scale circulation follows present-day conditions, while mesoscale dynamics and thermodynamic processes evolve freely (Sánchez-Benítez et al. 2022; Pithan et al. 2023). In the context of land-atmosphere interactions, this setup enables a detailed, isolated investigation of the thermodynamic effects of climate change, ignoring, however, the possible influence of land-atmosphere interactions on the global circulation.

The global storyline simulations are constructed by branching from the corresponding historical and SSP370 CMIP6 simulations previously produced with AWI-CM1 (Semmler et al. 2020). Branching is performed from model states when the respective global warming levels (GWL) are reached, determined using an 11-year centered moving average (Sánchez-Benítez et al. 2022). Accordingly, the global storylines are initialized on 1 January 1851, 2017, 2038, 2065, and 2093, representing pre-industrial (+0 K), present-day (+1.4 K), +2 K, +3 K, and +4 K warming levels, respectively (Sánchez-Benítez et al. 2022; Klimiuk et al. 2025). Five realizations of the CMIP6 simulations yield five ensemble members for each nudged storyline (Semmler et al. 2020; Sánchez-Benítez et al. 2022). To summarize, the simulations span the period 2017–2022 (2017 is considered as spin-up) and include five warming levels, each represented by a five-member ensemble.

The performance of AWI-CM1 falls within the range of CMIP6 models: the performance indices over northern mid-latitudes ($30-60°$N), reflecting the absolute error in climatology for 1989–2014 of the historical simulation as a fraction of the absolute error averaged over CMIP6 models (for the metric description see Streffing et al. 2022), are shown in Figure S1. For June-August, the performance indices of near-surface temperature (tas) and precipitation (pr) are 0.79 and 0.93, respectively. We conclude that AWI-CM1 is representative of its class and an appropriate choice for our regional storyline experiments. A major advantage of using a coupled model to generate global storylines is that the lower boundary conditions - sea surface temperature (SST) and sea-ice concentration (SIC) - do not need to be prescribed separately, and no assumptions about their increments are required. This differs from storyline approaches based on prescribed SST and SIC anomalies (e.g., Wehrli et al. 2020; Garderen et al. 2021).

The global AWI-CM1 storylines provide initial and boundary conditions for dynamical downscaling using the regional ICON-CLM model (ICOsahedral Nonhydrostatic model in the Climate Limited-area Mode, Zängl et al. 2015; Pham et al. 2021). Specifically, we utilized the ICON version 2.6.5.1 and the SPICE v2.0 runtime environment (Rockel and Geyer 2022). The full set of global storylines described above was downscaled over the EURO-CORDEX domain at a horizontal resolution of 12 km (for domain description, see e.g., Jacob et al. 2014). The soil initialization was based on ERA5 soil moisture and soil temperature datasets at all warming levels. To ensure a sufficient spin-up time for the soil variables, the year 2017 was run twice for pre-industrial, +2K, +3K, and +4K storylines (see Klimiuk et al. 2025). In addition to the storyline simulations, we produced a control ICON-CLM simulation for the same period 2017–2022 driven by ERA5 for evaluation purposes.

The land-surface processes in ICON-CLM are represented by the TERRA module (Doms et al. 2021). In the configuration used for this study, TERRA incorporates seven hydrologically active layers (up to the depth of 7.2 m) and an additional climatological layer that provides the lower boundary condition. This boundary condition is defined by the annual mean 2 m-temperature, which constrains the bottom soil layer thermodynamically, while a gravitational drainage condition governs the soil moisture below the lowest level (Doms et al. 2021).

Bare soil evaporation in TERRA is represented using a resistance-based approach described in Schulz and Vogel (2020). Plant transpiration is based on the two-resistance concept introduced by Dickinson (1984) and follows the implementation described in Doms et al. (2021). The parametrization of evapotranspiration in TERRA does not explicitly incorporate a critical soil moisture threshold; however, the foliage resistance expressed following Dickinson (1984) combines several empirical resistance factors (F-Functions, see Doms et al. 2021) describing the influence of radiation, soil moisture, ambient temperature, and ambient specific humidity on the stomatal resistance.

2.2 Theoretical framework of soil moisture regimes

To identify the soil moisture regime, we use the $EF(\theta)$ framework (Seneviratne et al. 2010; Schwingshackl et al. 2017, 2018; Feldman et al. 2019) that can be described as follows (see Fig. 1):

$$EF(\theta) = \begin{cases} 0, & \text{if } \theta < \theta_{wilt} \\ EF_{max}\frac{(\theta-\theta_{wilt})}{(\theta_{crit}-\theta_{wilt})}, & \text{if } \theta_{wilt} \leq \theta \leq \theta_{crit} \\ EF_{max}, & \text{if } \theta > \theta_{crit} \end{cases} \quad (1)$$

where $EF = \frac{\lambda E}{R_n}$ is the evaporative fraction, defined as a ratio of latent heat flux λE to the net radiation flux R_n at the surface. θ_{wilt} is the wilting point at which the soil only contains the water strongly bound to the soil matrix, inaccessible to plant transpiration. θ_{crit} is the critical soil moisture below which the evapotranspiration becomes limited by the water availability. EF_{max} is the maximal feasible

evaporative fraction. In case of $\theta > \theta_{crit}$, the evapotranspiration regime is energy-limited, and for $\theta < \theta_{crit}$, the regime is moisture-limited (see Fig. 1).

It has been shown that both root-zone and surface soil moisture can be used for the identification of evapotranspiration regimes, despite the high relevance of the root-zone soil moisture for the plant evapotranspiration (Qiu et al. 2016; Schwingshackl et al. 2017; Dong et al. 2022). In this study, we consider the upper three soil layers (0–9 cm) to define evapotranspiration regimes, as we found the clearest distinction between the two regimes for this depth, and 9 cm corresponds best to the typical thickness of the surface layer in observations and reanalyses. We estimate the critical soil moisture by applying a piecewise linear regression model to data aggregated from May to September across all five climates and five ensemble members. Consistent with previous studies (e.g., Schwingshackl et al. 2017; Feldman et al. 2019), we allow for a non-zero slope in the energy-limited regime. To further support our choice, we tested both piecewise linear fit methods, without constraining the right slope to zero and with this constraint. The first method fits the data slightly better (see Figure S2a) and yields the breakpoint values that are on average 0.02 mm^3/mm^3 lower than those obtained by the second method (see Figure S2b). Before fitting, we discard the data points with an evaporative fraction (*EF*) larger than one and with negative values of surface fluxes. For the resulting regressions, we only allow the slope in the moisture-limited regime to be positive and greater than the slope in the energy-limited regime.

Critical soil moisture depends not only on the soil characteristics but also on the local surface energy balance, and may therefore be non-stationary under global warming (Hsu and Dirmeyer 2023b). To assess whether θ_{crit} differs among the storyline simulations for different GWLs, we first compute θ_{crit} separately for each GWL. Figure S2c shows a slight decrease in θ_{crit} with increasing GWL, resulting in a mean difference of less than 0.01 mm^3/mm^3 between the pre-industrial and +4 K climates over the EUR region. It is noteworthy that such a small decrease can be detected in the storyline simulations, likely because the constrained large-scale atmospheric circulation strongly reduces the impact of dynamical (internal) variability of the results. Nevertheless, the magnitude of this change may be small enough to be outweighed by the internal variability that would be present in free-running simulations. It may also reflect a fitting artefact, as the estimated breakpoint can be sensitive to the distribution of data points along the relationship. In particular, a greater concentration of points on the dry side may bias the least-squares fit toward lower soil moisture values. Further work is needed to clarify this tendency, in particular by exploring alternative methods for breakpoint estimation. Within the scope of this study, we therefore determine critical soil moisture by combining all GWLs and all ensemble members. We compute θ_{crit} separately for each year and obtain the final estimate by averaging these annual values. Combining the simulations across all GWLs increases the spatial coverage of valid piecewise linear regressions.

Another metric that captures the same underlying mechanism is the correlation between soil moisture θ and latent heat flux λE (e.g., Santanello et al. 2018; Rousi et al. 2023). In the energy-limited regime, this correlation tends to be close to zero or negative. Conversely, a positive correlation indicates that soil moisture availability is the limiting factor for evaporation. To account for the variability in evapotranspiration, we scale the correlation by the standard deviation of the latent heat flux $\sigma_{\lambda E}$, following Santanello et al. (2018) and Dirmeyer (2011). Accordingly, the resulting metric provides a measure of the coupling strength ($C_{\theta E}$) between soil moisture and evapotranspiration:

$$C_{\theta E} = \sigma_{\lambda E} \rho(\lambda E, \theta) \tag{2}$$

2.3 Quantification of the temperature response: warming amplification

It has been previously shown that the 2 m-temperature in regional storylines over Europe is linearly dependent on the global warming level (Wehrli et al. 2020; Vries et al. 2024; Klimiuk et al. 2025). Thus, the response of 2 m-temperature to climate change can be reflected as the temperature increment per degree of background warming. This metric was referred to as the "warming rate (WR)" in Klimiuk et al. (2025) or the "temperature response factor (TRF)" in Vries et al. (2024). In this study, we define it as "warming amplification" (WA) and compute it at each grid point and for each day by fitting a linear least-squares regression of daily maximum temperature (TX) against global warming level (GWL):

$$WA = \frac{\Delta TX}{\Delta GWL} \tag{3}$$

2.4 Model evaluation and study areas

For the evaluation of near-surface temperature and precipitation, we used E-OBS (v28), a daily gridded, land-only observational dataset for Europe (Cornes et al. 2018; Copernicus Climate Change Service 2024) and both ERA5 and ERA5-Land reanalyses datasets (Hersbach et al. 2020; Muñoz-Sabater et al. 2021).

For the evaluation of latent and sensible heat fluxes, we used station data from the Integrated Carbon Observation System (ICOS; Icos Ri et al. 2025) at two locations: Juelich

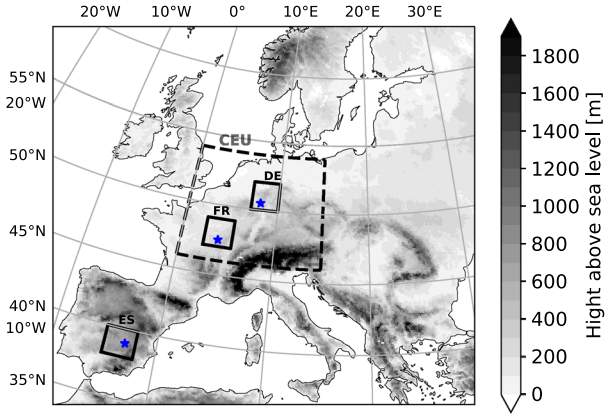

Fig. 2 Height above sea level in the region of interest. Study subregions are outlined with solid black lines: DE - Germany, FR - France, ES - Spain. The dashed box outlines the Central-European (CEU) subregion. Blue stars are the exemplary grid points used in Fig. 7

Selhausen in Germany (DE-RuS, 50.865906°N, 6.4471445°E, data available for 2019–2022) and Fontainebleau-Barbeau in France (FR-Fon, 48.476357°N, 2.780096°E, data available for 2020–2022). These sites were selected based on the availability of ICOS data and their relevance to the study area. The ICOS data at the DE-RuS station were augmented by the TERENO dataset for the year 2018 (Zacharias et al. 2024). Additionally, soil moisture was compared with SMAP Level-3 satellite observations (Entekhabi et al. 2016) over selected regions in France and Spain (see Fig. 2). For completeness, two reanalysis datasets were also included: ERA5 (Hersbach et al. 2020) and GLEAM4 (Global Land Evaporation Amsterdam Model; Miralles et al. 2011, 2025).

For large-area averages over Central Europe, we consider a subregion encompassing Germany, France, Belgium, the Netherlands, and Luxembourg, bounded by 0°W-15°E longitude and 46°N-54°N latitude (CEU, see Fig. 2). A country mask was applied to the data to consider only the data points located over the countries mentioned above. The statistical analyses of the temperature response presented in Section 4 were conducted over three subregions located in Germany (DE), France (FR), and Spain (ES), as illustrated in Fig. 2. Finally, to exemplify the soil moisture-evapotranspiration relationship, we selected three grid points within these subregions, ensuring that their soil type is loam, as this soil type is most prevalent in the investigated region. Finally, to assess the dependence of WA on the presence or absence of a soil moisture regime transition, we consider a larger region spanning 10°W - 30°E longitude and 35°N - 65°N latitude (EUR).

3 Results

3.1 Overview of the studied period and model evaluation

To gain a better picture of the soil conditions during the 2018–2022 hydrological period (October 2017 to September 2022), we considered the anomalies of the full-column soil moisture (0–289 cm, Fig. 3a) and surface soil moisture (0–7 cm, Fig. S3) based on ERA5-Land, as well as precipitation based on E-OBS (Fig. 3b). We considered daily climatologies for the period 1988–2017 as a basis for computing anomalies for the period 2018–2022. The heat and drought series began with a drastic decline in precipitation and soil moisture in June 2018 (Fig. 3a,b, see also Rousi et al. 2023). Unlike the surface soil moisture, the soil moisture in the deeper layers did not recover over the winter of 2018/2019 (Fig. 3a), leaving the following year, 2019, to be anomalously dry (Fig. 3a and Fig. S3). Also in 2020, the soil moisture remained mostly below the climatology, even though precipitation remained above average in winter and spring. The year 2021 was the wettest in the considered period, with substantial positive precipitation anomalies and extremes, especially in mid-summer (see e.g., Mohr et al. 2023; Ludwig et al. 2023). The year 2022 experienced a similar soil moisture deficit to that in 2018–2020, with

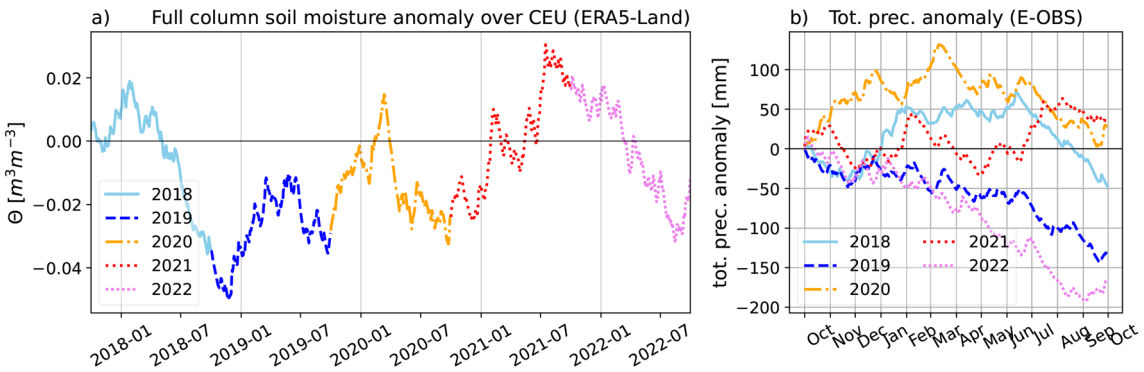

Fig. 3 Daily anomalies relative to the 1988–2017 climatology over the CEU region (as defined in Fig. 2) for **a** full-column soil moisture from ERA5-Land and **b** total precipitation from E-OBS. Colors indicate the hydrological years beginning in October of the previous calendar year

substantial negative precipitation anomalies (Fig. 3 and Fig. S3). The 2022 drought reached unprecedented severity across Central, Western, and Southern Europe, and, due to accumulated legacy effects over the multi-year drought period, inflicted significant damage on ecosystems (e.g., Knutzen et al. 2025).

The representation of 2 m-temperatures in our present-day regional storylines was extensively evaluated in Klimiuk et al. (2025). For Central Europe, the RMSD to E-OBS is 1–2 K for the daily mean 2 m-temperature and 2–3 K for the daily maximum 2 m-temperature (see Fig. S5 in Klimiuk et al. 2025). Figure S4 shows an overall good agreement of the time series of daily maximum 2 m-temperature (TX) over Central Europe (CEU subregion in Fig. 2) during May-September of each modelled year obtained by our regional storylines and the ICON control simulation driven by ERA5 in comparison to E-OBS, ERA5, and ERA5-land.

Figure S5 shows the comparison of present-day daily accumulated precipitation over the same domain by the regional present-day storyline ensemble and the ICON control simulation compared to ERA5 and E-OBS. The control simulation driven by ERA5 tightly follows the observations, whereas some overestimation of the accumulated precipitation can be seen for the present-day storyline simulations, when compared to E-OBS. This overestimation is inherited from the global AWI-CM1 model, which imposes a positive bias in atmospheric moisture entering the regional domain (not shown).

Figure 4 shows a comparison of simulated latent (Fig. 4a) and sensible (Fig. 4b) heat fluxes with the in situ observations and reanalysis products described in Sect. 2.4 at the FR-Fon (Fontainebleau-Barbeau, France) and DE-RuS (Selhausen, Juelich, Germany) sites. Both the regional present-day ICON storyline and the ICON-control simulations are in good agreement with the reanalyses and the station observations. The temporal correlation of the ICON simulations with ERA5 (brown numbers in Fig. 4) is higher than that with the station observations (blue numbers in Fig. 4), likely reflecting differences in spatial representativeness between gridded products and point-scale measurements.

Figure S6 compares simulated soil moisture and turbulent heat fluxes over the DE, FR, and ES subregions. For soil moisture, the SMAP Level-3 satellite product serves as an observational reference for the FR and ES subregions (Fig. S6d,g), whereas no corresponding observational data are available for DE because of insufficient satellite data quality. The good agreement in mean values and the high correlations with both observations and reanalyses further support the realism of the regional ICON simulations over the study area.

3.2 Temperature response to global warming

We exemplify the quantification of the WA (see Sect. 2.3) based on the hottest day of 2018 in Central Europe in the ensemble of ICON storylines (see Fig. 5). According to Fig. 5f, the WA exceeds 3 KK^{-1} over large parts of Central and South-Eastern Europe; however, the spatial pattern of the response does not immediately mimic the temperature pattern in Fig. 5b. Klimiuk et al. (2025) hypothesized that land-atmosphere feedbacks act differently at different locations within the domain, resulting in the spatial variability of the WA. It should be noted that the grid-point-wise interpretation of the thermodynamic response is a necessary simplification, even though the large-scale circulation is nudged: coupling between mesoscale dynamics and the land-atmosphere interface may introduce additional variability in TX at a given grid point.

Even when averaging over subregions of interest, we still see evidence of a different response to high-temperature

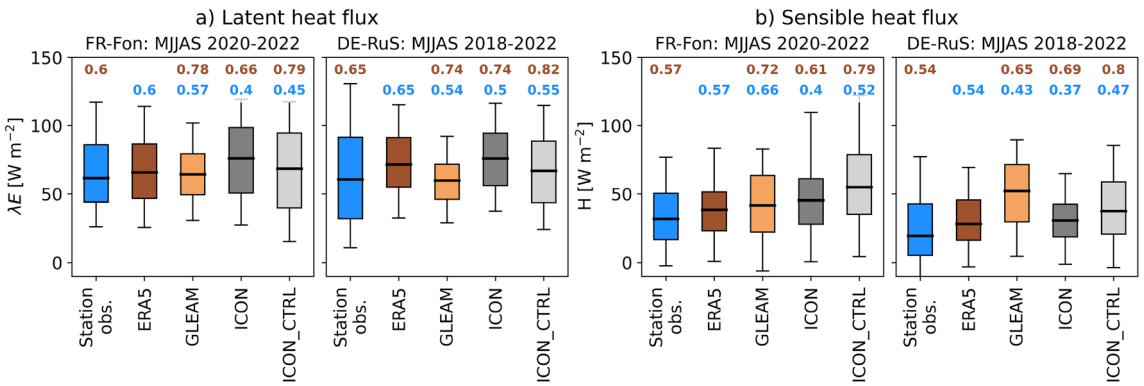

Fig. 4 Comparison of daily mean values of (a) latent heat flux and (b) sensible heat flux at two ICOS stations: FR-Fon (Fontainebleau-Barbeau, France; 48.4764°N, 2.7801°E) and DE-RuS (Selhausen Juelich, Germany; 50.8659°N, 6.4471°E). The periods of data availability are indicated in the respective figure titles. The brown (upper) numbers over each box indicate the temporal correlation of each dataset with ERA5. The blue (lower) numbers indicate the temporal correlation of each dataset with the station observations. The box boundaries correspond to the 25th and 75th percentiles, the whiskers correspond to the 5th and 95th percentiles of the data, and the horizontal lines represent the median

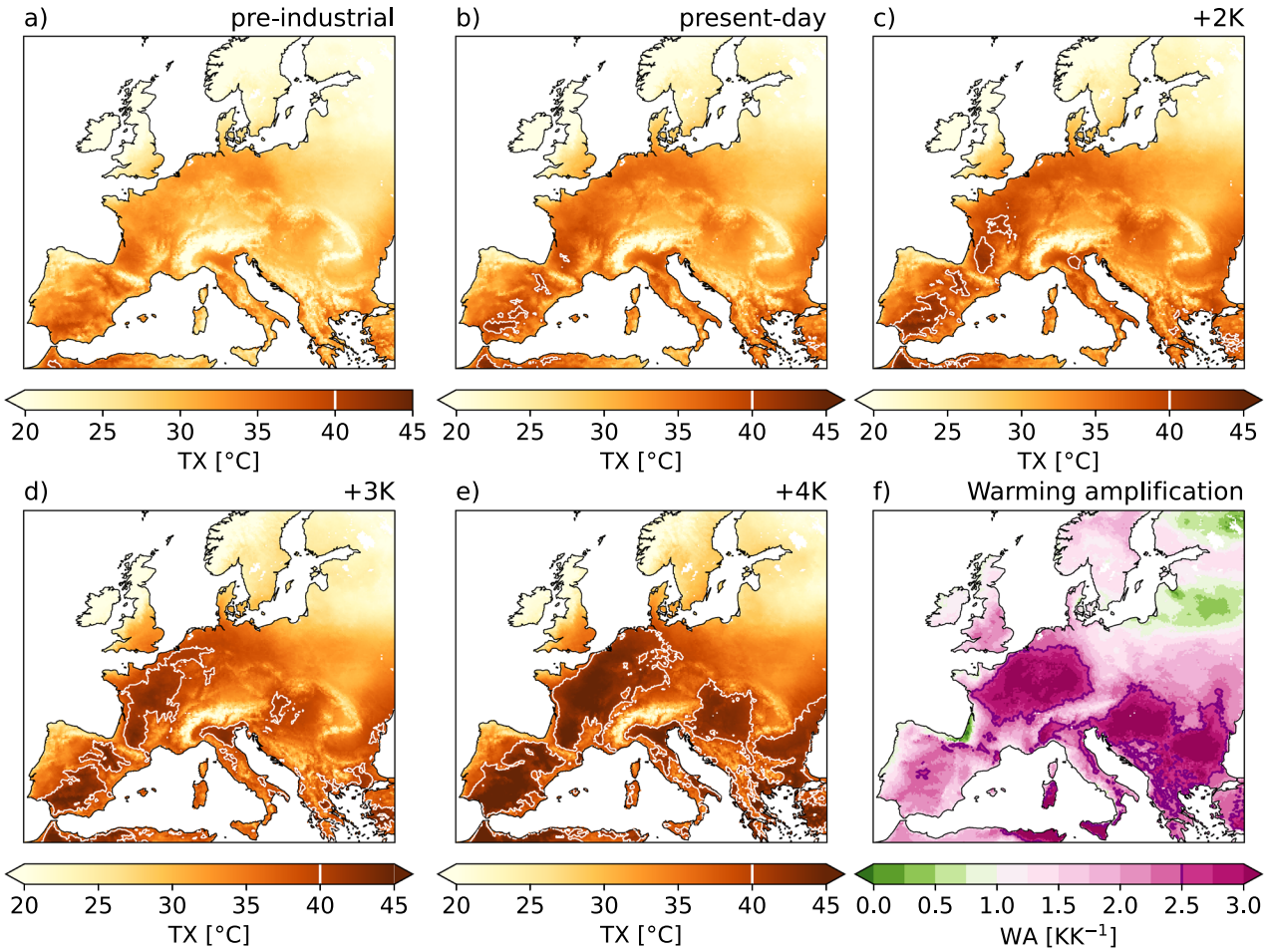

Fig. 5 **a-e** Ensemble mean of the Maximum 2 m-temperature on 7 August 2018, the hottest day of 2018 over the CEU subregion, as simulated by ICON EUR-12 storylines corresponding to (**a**) pre-industrial, (**b**) present-day (+1.4 K), (**c**) +2 K, (**d**) +3 K, and (**e**) +4 K global warming levels. **f** Regional warming amplification (WA) on that day, defined as the slope of the linear regression of daily maximum 2 m-temperature against global warming level

extremes. For example, Figure S7b shows that, despite the high temporal correlation between TX and WA of 0.65 over CEU in summer 2019, a distinct peak of daily maximum temperature on the 25th of July led to only a moderate WA, whereas the local temperature maximum in late August coincides with a peak of WA (the days indicated by the solid black and dashed green lines in Fig. S7b). Moreover, the WA in the semi-arid ES subregion shows almost no correlation with TX (see Figure S8).

To determine whether the distinction in WA seen in Figs. 5, S7, and S8 can be generalized, we examine the statistical relationship between WA and TX. Figure 6a-c shows the WA in May-September w.r.t present-day TX over the full modelled period (2018–2022) for the three subregions defined in Fig. 2 (a similar analysis was done by Vries et al. (2024) for the Netherlands). In all considered subregions, the response of lower TX scales equal to the background warming level, resulting in average WA close to unity. It is followed by a growth of WA that reaches 2 KK^{-1} on average. This growth saturates over DE and FR subregions at TX values of 36-40°C (Fig. 6a-b), whereas over the ES subregion, WA shows stabilization at TX values of 24-28° C (Fig. 6c).

Note the large spread of the possible WA values in DE and FR subregions at the present-day temperature range of 32–36 °C (Fig. 6a-b), which implies a strong variability of the response. Considering that WA is usually lower in June in Central Europe (Fig. S7), it is reasonable to suggest that the lower part of the response distribution originates from the early summer days. This can be confirmed by Fig. 6d-e, where the cyan contour delineates 95% of WA for June 2018–2022. With the drying of the soil towards late summer, the WA in August accommodates the upper part of the distribution (red contour in Fig. 6d-e). July, as shown by the orange contour in Fig. 6d-e, exhibits variable responses, mostly lying between those of June and August. The highest

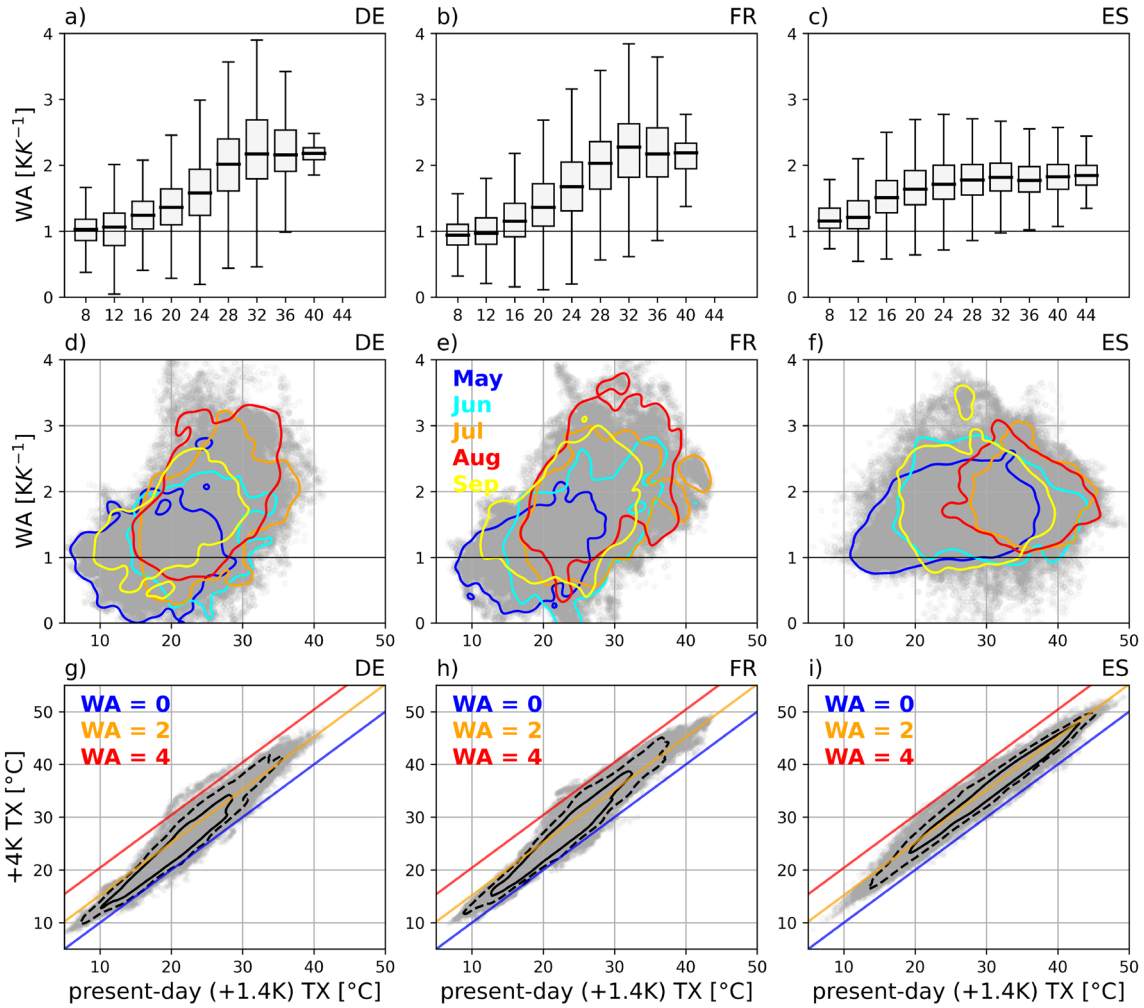

Fig. 6 **a-c** Warming amplification (WA) as a function of present-day TX. **d-f** Scatter plots of WA versus present-day TX, with colored contours indicating the 95th percentile for each month in the May-September period. (g-h) Scatter plots comparing present-day and corresponding +4 K daily maximum TX values within the DE, FR, and ES subregions. The dashed black contour denotes the 95th percentile, and the solid black line marks the 75th percentile of the data

temperatures display an average WA of 2 KK^{-1}. Such high variability in the values of WA emphasizes the tendency of present-day late summer moderate temperatures to turn into extreme heat events, increasing the probability of heatwaves in late summer (especially in August) over Central Europe.

Finally, Fig. 6g-i gives additional insights into what WA actually means for the future summer temperatures: we show the absolute values of TX in +4 K climate plotted against TX in the present-day climate (see Fig. 6g–i). For the FR and DE subregions, most present-day events with temperatures of 36-37°C would exceed 40°C in a +4 K climate. The average share of days exceeding 40°C increases from 0.5 to 4 % in the FR subregion and from 0.02 to 1.2 % in the DE subregion (see also Table 1 in the Supplementary material). For the ES subregion, the share of days over 40°C would increase from 6 to 29 %. The orange line in Fig. 6g-i corresponds to WA equal to 2.0 KK^{-1}. Converging around this line, the values of the daily maximum 2 m-temperature reach 45°C, 48°C, and 51°C in +4 K climate over DE, FR, and ES subregions, respectively. The 99th percentile of the daily maximum temperatures grows with the rate of 2.2 KK^{-1} reaching 40.4°C over the DE subregion, with the rate of 2.3 KK^{-1} reaching 44.2°C over the FR subregion, and with the rate of 1.9 KK^{-1} reaching 47.9°C over the ES subregion (see Table S1 in the Supplementary material).

Overall, these results show that thermodynamic warming amplification systematically shifts present-day extreme heat events toward much hotter and more frequent extremes, pushing large parts of Western and Central Europe into temperature ranges that are currently rare or unprecedented. At the same time, extremely hot and dry events exhibit still high but limited WA. In the next section, we examine in more detail possible mechanisms underlying the differing WA across all summers of the considered period.

3.3 Evapotranspiration regimes based on the $EF(\theta)$ framework for different global warming levels

After providing a general overview of temperature responses, we will now examine the nature of the high variability of WA in Central Europe. We hypothesize that the change in the strength of soil moisture-temperature coupling with increased background warming plays a crucial role in the magnitude of WA.

Figure 7 shows the evaporative fraction (*EF*) as a function of the surface soil moisture (θ) for the summer of 2019 at three selected grid points identified in Fig. 2 (other summers are shown in Fig. S9 - S12 of the Supplementary material). Here, we consider each ensemble member separately, meaning that each day is represented by five points in the scatter plots. We additionally color-coded the points corresponding to each month for the period between May and September.

The evapotranspiration regime is energy-limited at the DE and FR grid points in early summer, as most data points in May and June are located on the plateau of the $EF(\theta)$ relationship (Fig. 7a-j). In the case of summer 2019, the soil moisture during most of July, August, and September is also in the energy-limited (wet) regime at the DE grid point in the pre-industrial climate (Fig. 7a). In contrast, the soil moisture at the FR grid point is mainly in the moisture-limited regime between July and September in the pre-industrial climate (Fig. 7f).

With increasing background warming, the July-September data points at the DE grid point move down along the slope of the $EF(\theta)$ relationship, causing most late-summer days to shift into a moisture-limited evapotranspiration

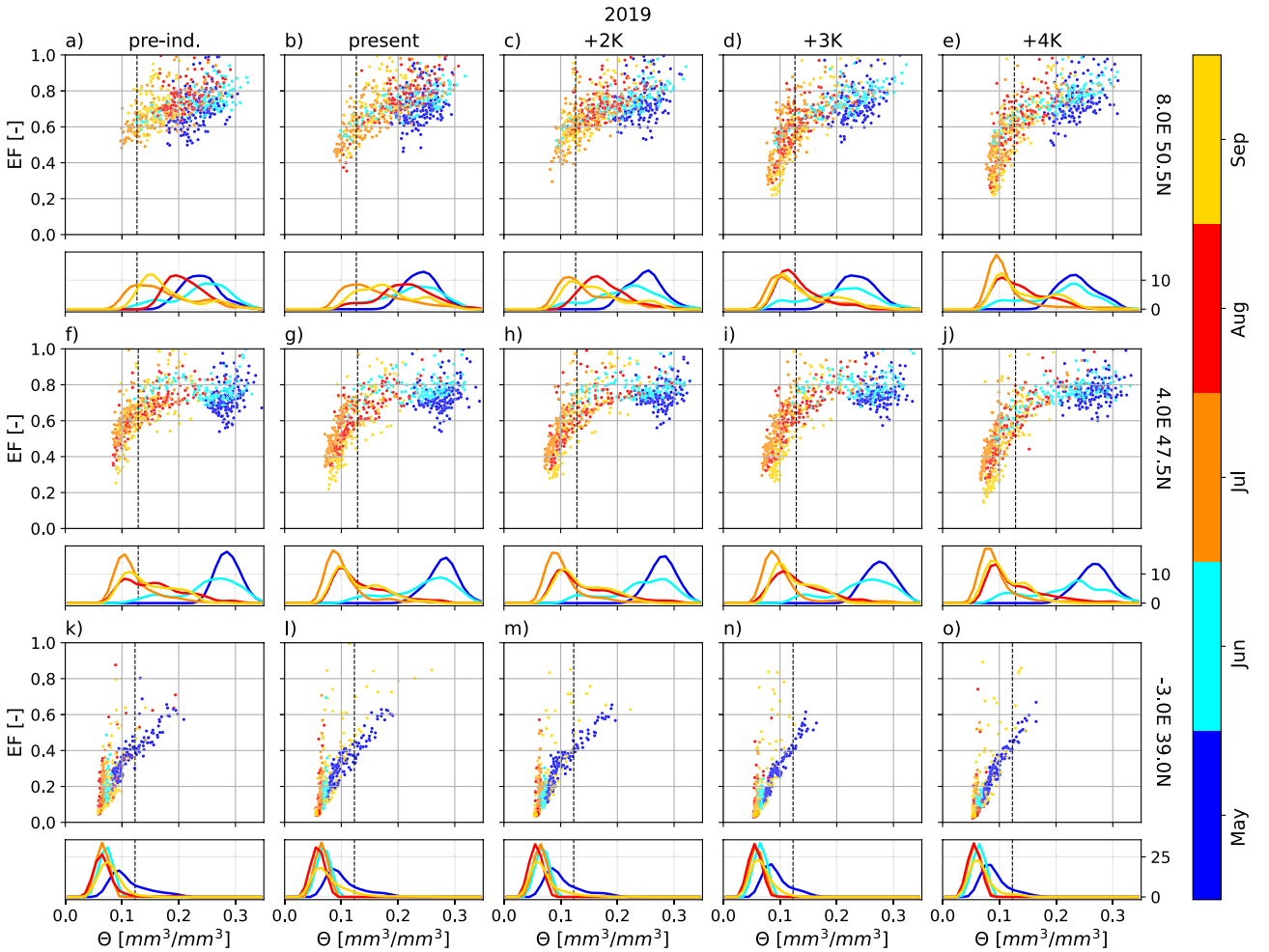

Fig. 7 Evaporative fraction (*EF*) as a function of volumetric soil moisture in the upper 9 cm for each climate for May-September 2019 at three grid points: **a-f** DE: 50.5°N, 8°E; (f-j) FR: 47.5°N, 4°E; (k-o) ES: 39°N, 3°W (see also blue stars in Fig. 2). The five ensemble members are shown independently, such as each day is represented by five data points. Each data point is color-coded by the month: blue - May, cyan - June, orange - July, red - August, and yellow - September. Beneath each panel, the marginal distribution of soil moisture is shown as a smoothed histogram-based estimate of the probability density function. The dashed vertical line corresponds to the value of critical soil moisture computed as described in Sect. 2.2

regime (Fig. 7b-e). In contrast, at the selected grid point in FR, most July-September days in 2019 are already characterized by a moisture-limited regime at lower warming levels; consequently, fewer points undergo a regime shift (Fig. 7f-j). Inspection of other years (Figs. S9-S12a-j) shows that, at both DE and FR grid points, May and June tend to remain energy-limited, whereas July-September shift toward the moisture-limited regime with increasing GWL. In 2022, which was exceptionally dry due to dynamical conditions and legacy effects from previous years, July-September are moisture-limited in the pre-industrial climate at both DE and FR grid points, and a large fraction of days in May-June also shift into the moisture-limited regime.

Due to an overall drier climate at the ES grid point, the soil already enters the moisture-limited regime in May in pre-industrial (Fig. 7k) and present-day (Fig. 7l) climates. Moreover, no substantial redistribution of the data points occurs with increasing GWL (see Fig. 7m-o, Fig. S9-S12m-o).

3.4 Investigating the connection between the evapotranspiration regime and temperature response

To assess in detail the connection between the evapotranspiration regime and temperature response, we first explore the $EF(\theta)$ relationship at two specific grid points on the hottest day of each year (vertical black lines in Fig. S7): the first grid point corresponds to the location within CEU exhibiting the highest TX, whereas the second point corresponds to the location within CEU exhibiting the highest WA on the same day (see Fig. 8). The location of both grid points is indicated by blue circles (the highest TX) and blue squares (the highest WA) in Fig. 9.

We aggregated all climates and months of the period between May and September (MJJAS) into one graphic. The dashed vertical line corresponds to θ_{crit} at that grid point computed based on the whole dataset (see Sect. 2.2). The data points highlighted by triangles correspond to the hottest day of the year and are color-coded, with each color representing the respective warming level (see caption of Fig. 8). TX over the grid point for that day is shown in the top-left corner, and the corresponding WA is shown in the bottom-left corner.

The contrast between the hottest grid-point and the grid-point with the highest WA is especially evident for the years 2019 (Fig. 8c vs. d), 2020 (Fig. 8e vs. f), and 2022 (Fig. 8i vs. j): in all three cases for the hottest grid point (Fig. 8c,e,i), the triangles, reflecting the evapotranspiration regime of the selected day (see legend in Fig. 8), start their path in the steeper, moisture-limited part of the $EF(\theta)$ relationship and "move" down along the slope with increasing global warming (blue triangle in Fig. 8 shows the state in the pre-industrial climate; dark-red triangle shows the state in the +4 K climate). The associated WA at those grid-points are close to 2.0 KK^{-1}. In contrast, the highlighted data points at the location of the highest WA (Fig. 8d,f,j) start at the flat, energy-limited part of the $EF(\theta)$ relationship, ending up in the moisture-limited part for the warmer climates. The associated WA at those grid-points is considerably higher and close to 3.0 KK^{-1}. For the case of 2018, the evapotranspiration regime can be identified as energy-limited in the pre-industrial climate in both chosen grid-points (Fig. 8a,b), and both WA values are close to 3.0 KK^{-1}. Regarding 2021, the hottest grid point remained close to the energy-limited part of the $EF(\theta)$ relationship, exhibiting the WA of 1.7 KK^{-1} (Fig. 8g), and the point of highest WA showed only minor movement towards the moisture-limited regime, with the WA of 2.1 KK^{-1} (Fig. 8h). Note that 2021 was the wettest year of the period (see Fig. 3; Mohr et al. 2023; Knutzen et al. 2025).

A similar behavior can be seen in Fig. S13, where the same analysis was performed for the day of the highest WA over CEU, marked by the dashed green vertical line in Figure S7. The WA values approaching and exceeding 3.0 KK^{-1} are accompanied by a transition of the evapotranspiration regime or at least a movement from the top of the $EF(\theta)$ slope to the bottom (Fig. S13b, d, f, h, j). In contrast, the hottest points with present-day soil moisture far below the critical value tend to respond with a lower WA (Fig. S13 a, c, e, g, i).

We estimated the critical soil moisture at each grid point as explained in Sect. 2.2 (see Fig. S14 of the supplementary material) and identified the evapotranspiration regime for each day of the summer season in each climate.

We now consider the spatial patterns of TX and WA on the hottest day of each year (see Fig. 9a, d, g, j, m; the hottest days are marked with the vertical black lines in Fig. S7). The right panel (c, f, i, l, o) in Fig. 9 shows whether a grid point shifted from the energy-limited into the moisture-limited evapotranspiration regime on that day in the +4 K climate, compared to the pre-industrial climate. For this and further analyses, a grid point is considered to have a regime transition on a specific day if at least one ensemble member is energy-limited in the pre-industrial climate and all ensemble members are moisture-limited in the +4K climate (EL-ML, dark red color in Fig. 9c,f,i,l,o). A grid point is considered to have no regime transition in the moisture-limited regime if the soil moisture is below the θ_{crit} both in pre-industrial and +4K climates for all ensemble members (ML-ML, light beige color in Fig. 9c, f, i, l, o). Finally, if the soil moisture in +4 K climate is above θ_{crit} in at least one ensemble member, disregarding the value in the pre-industrial climate, the grid point is considered to retain the

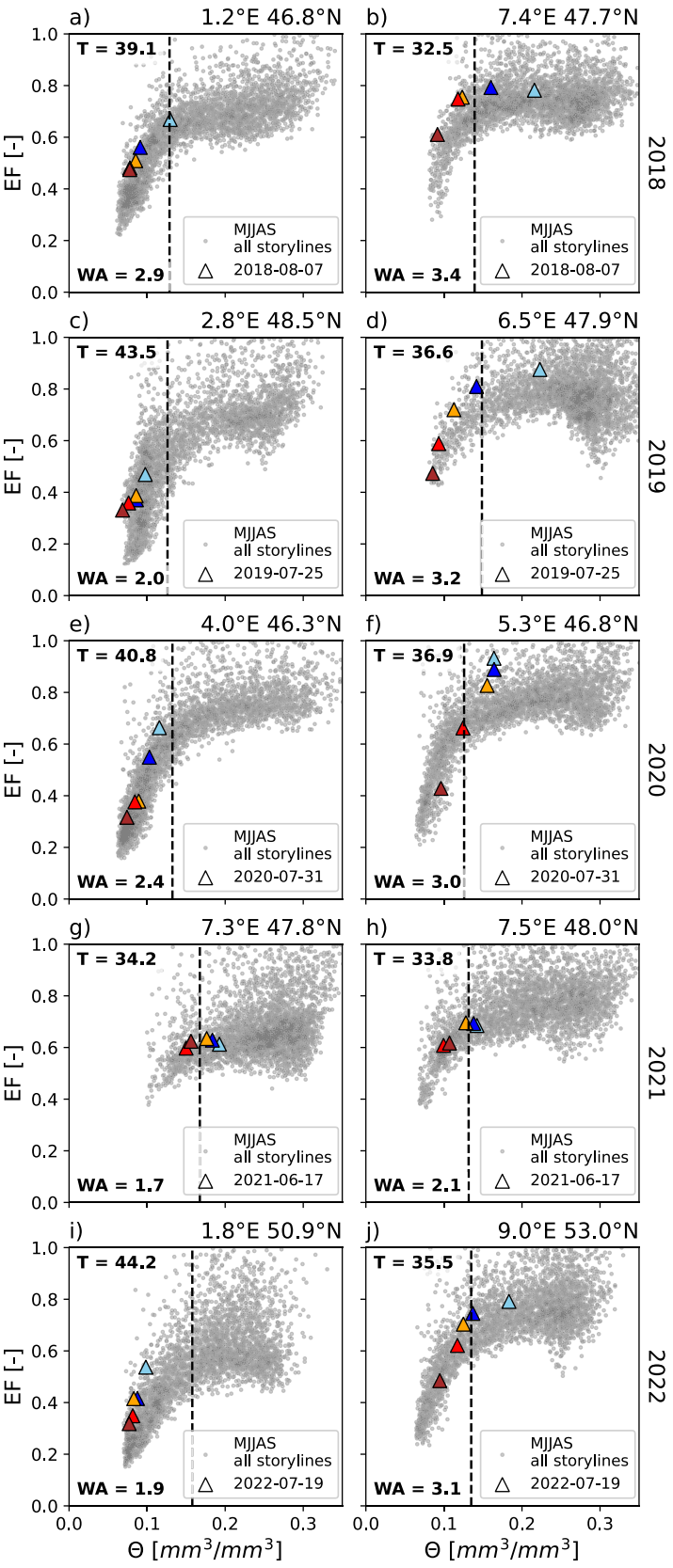

Fig. 8 Scatter plots of evaporative fraction (*EF*) versus volumetric soil moisture (θ), aggregated across all warming levels. The left column (a,c,e,g,i) shows data at the hottest location on the hottest day (blue circles in Fig. 9); the right column (b,d,f,h,j) shows data at the location with the highest WA on that day in the CEU domain (blue squares in Fig. 9). Colored triangles indicate the hottest day of the year. Colors correspond to the respective climate: pre-industrial (light blue), present-day (blue), +2 K (orange), +3 K (red), +4 K (dark red)

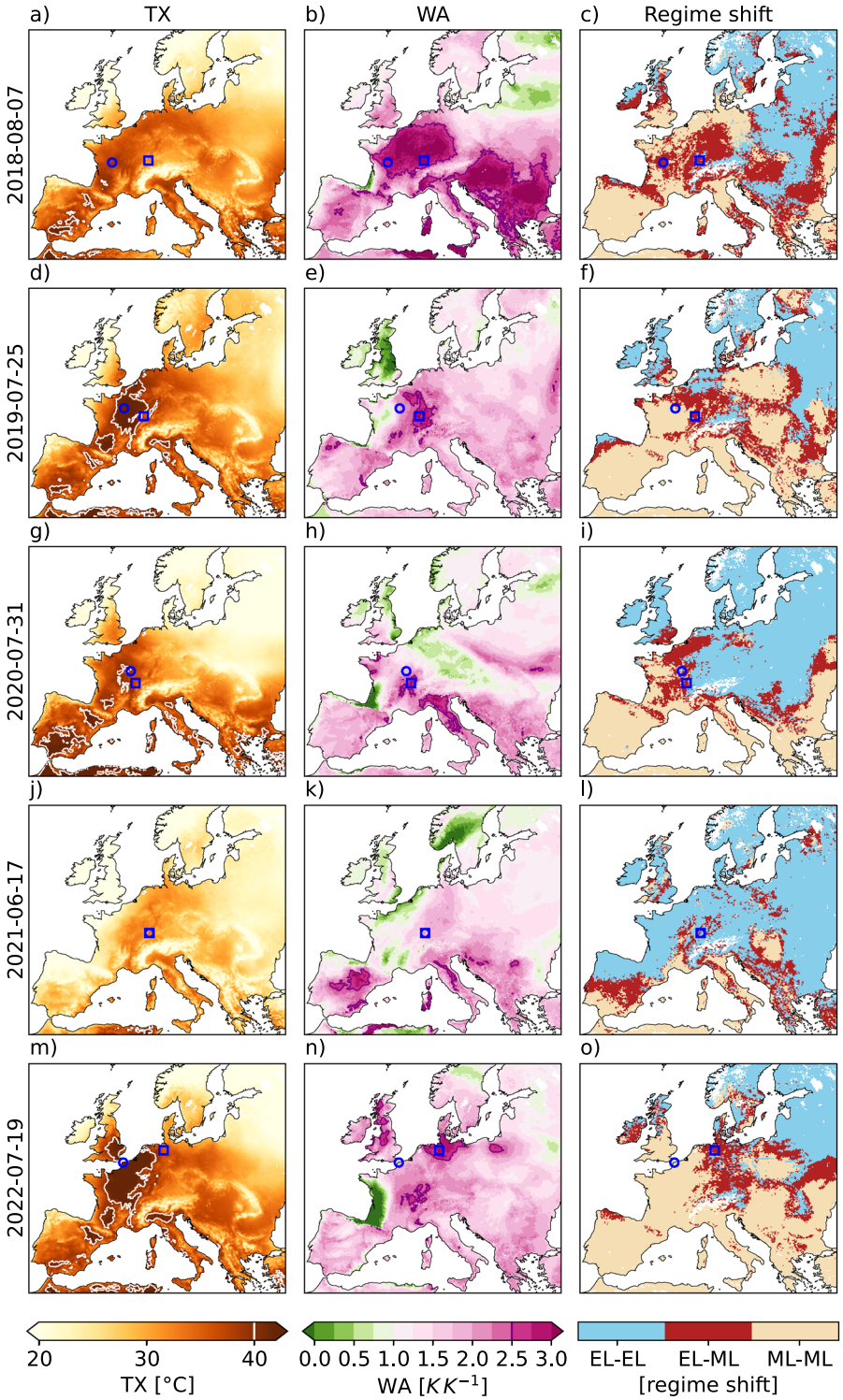

Fig. 9 (left column: a,d,g,j,m) Present-day maximum 2 m-temperature, (middle column: b,e,h,k,n) associated WA, and (right column: c,f,i,l,o) regime transitions on the hottest day of the year (the hottest day is defined as the annual maximum over the CEU subregion, see Fig. S7); "EL-EL" - the regime remained energy-limited, "EL-ML" - the regime was energy-limited in the pre-industrial climate and became moisture-limited in the +4K climate, "ML-ML" - the regime remained moisture-limited. The blue circle marks the grid-point with the highest temperature, and the blue square marks the grid-point with the highest WA over the CEU subregion

energy-limited regime (EL-EL, blue color in Fig. 9c, f, i, l, o).

In all cases except June 17, 2021 (Fig. 9j-l), where the hottest day remained well below 40°C, the pattern if WA does not coincide with the pattern of TX (Fig. 9b, e, h, n). In fact, Fig. 9c, f, i, l, o supports the hypothesis that the regions with high WA tend to exhibit an evapotranspiration regime transition, whereas the areas with higher TX and smaller WA show little to no regime transitions. Similar results were obtained for the day of the highest WA over CEU (see Fig. S15).

Figure 10a presents the change in the percentage of moisture-limited days in July and August 2018–2022 between the +4 K climate and pre-industrial conditions. It shows that in Central and Western Europe, over 50 % of days in July and August shift towards the moisture-limited regime in the warmer climate under similar circulation conditions. This implies an intensification of previously weak soil moisture-temperature coupling and an associated growth of the near-surface temperature variability. In contrast, the Central and Southern Iberian Peninsula experiences a negligible change in the number of moisture-limited days due to the already moisture-limited conditions in late summer in the present-day climate (Fig. 10a).

We also examine this coupling from a complementary perspective by analyzing changes in the coupling metric $C_{\theta E}$ (as defined in Eq. 2; see Fig. 10b). Regions exhibiting a strong positive change in $C_{\theta E}$ (Central Europe, Pyrenees, Balkans, and Carpathians in Fig. 10b) indicate an enhanced role of soil moisture-temperature coupling in modulating late-summer temperatures in future climate scenarios. Conversely, a negative change in this metric suggests a weakening of this coupling under global warming, particularly in the Mediterranean region (Fig. 10b). The marked contrast between Southern Europe and the rest of the domain arises from both a strong decrease in latent heat flux variability and a slightly less pronounced reduction in the correlation $\rho(\theta, \lambda E)$ (Fig. S16a-b). This likely reflects a decline in soil moisture availability, which becomes insufficient to exert a strong control on the latent heat flux variability (see, e.g., Miralles et al. 2012). Over Central and Eastern Europe, especially in elevated terrain, $\rho(\theta, \lambda E)$ increases markedly and is accompanied by higher values of the latent heat flux variability (see Fig. S16a-b).

The third variable closely linked to the prevailing soil moisture regime is the diurnal temperature range (DTR). In the moisture-limited regime, reduced evaporative cooling from morning to afternoon leads to an increase in DTR (Verdecchia et al. 1994; Dai et al. 1999; Bateni and Entekhabi 2012; Cattiaux et al. 2015; Feldman et al. 2019; Panwar et al. 2019; Paul et al. 2024). The extension of the diurnal temperature range also implies that the response of daily maximum temperatures to the background warming is larger than that of the minimum temperatures. This can be confirmed by the results of Vries et al. (2024) and Klimiuk et al. (2025), who found that the WA of daily maximum temperatures is higher than that of daily minimum temperatures in late summer.

A strong spatial correlation between the average DTR change and the number of shifts to the moisture-limited evapotranspiration regime (Fig. 10a and Fig. 10c) emphasizes the connection between both metrics. However, a non-negligible increase in DTR is still seen in the drier areas that did not show regime shifts, such as the Iberian Peninsula (Fig. 10c). Since the DTR is closely connected to land surface energy partitioning through the variability of the sensible heat flux (Schwingshackl et al. 2017; Panwar et al. 2019; Feldman et al. 2019), it continues to increase as soil moisture moves further down the slope of the $EF(\theta)$ relationship. This can partially explain the magnitude of the stabilized WA in already hot and dry regions, as seen in Fig. 6.

Figure 11 aggregates all daily WA values at each grid point over Europe grouped by three regime-transition cases: evapotranspiration regime transition (EL-ML), the retention of the moisture-limited regime (ML-ML), and the retention of the energy-limited regime (EL-EL). Our results clearly illustrate that the days that undergo a transition into the moisture-limited regime exhibit systematically higher WA than those that retain their evapotranspiration regime, and the WA on the days that remained energy-limited are smaller than those of the days that remained moisture-limited.

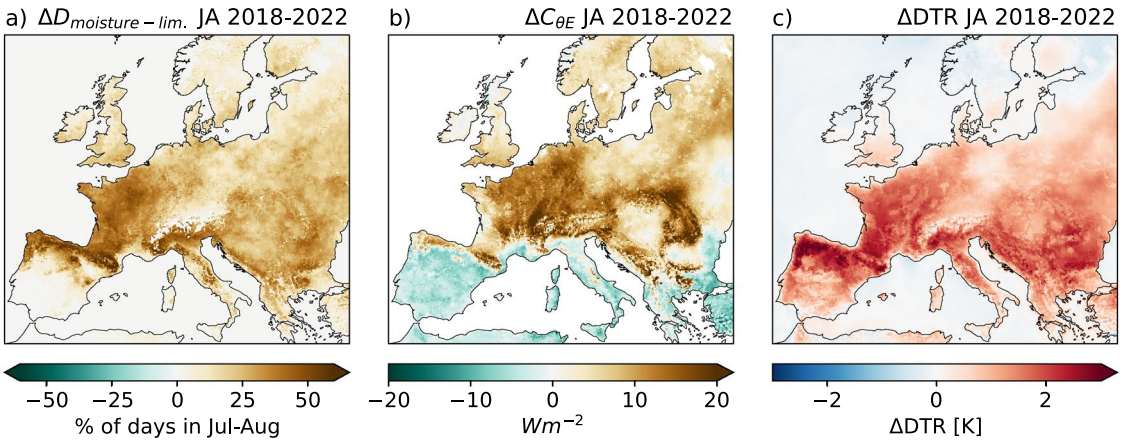

Fig. 10 Changes between the pre-industrial and +4 K climates for July-August 2018–2022 in (a) the percentage of days in the moisture-limited evapotranspiration regime, (b) $C_{\theta E}$, a scaled correlation coefficient between soil moisture and latent heat flux (defined in Eq. 2), and (c) diurnal temperature range (DTR)

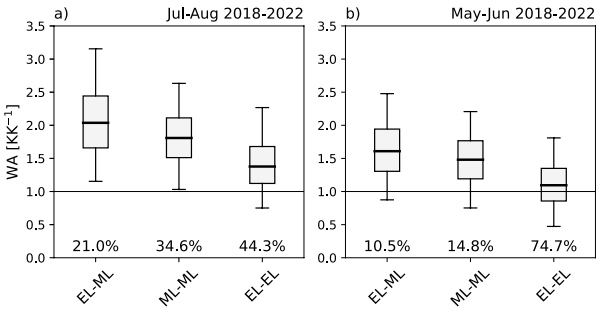

Fig. 11 Box-plots of warming amplification (WA) conditioned by three evapotranspiration regime transition cases: transition from energy-limited to moisture-limited regime (EL-ML), no transition within the moisture-limited regime (ML-ML), and no transition within the energy-limited regime (EL-EL) between pre-industrial and +4K climates for **a** July-August 2018-2022 and **b** May-June 2018-2022 over land in Europe. The box boundaries correspond to the 25th and 75th percentiles, the whiskers correspond to the 5th and 95th percentiles of the data, and the horizontal lines represent the median. The relative amount of data points satisfying each condition is given in percent under the boxes. All daily data points within 10°W-30°E longitude and 35°N-65°N latitude are taken into account

Thus, Fig. 11a summarizes our findings addressing the question of the connection of evapotranspiration regimes and the temperature response: (1) the highest WA is found for the cases with the regime transition, (2) the moderate WA is found for the cases where the evapotranspiration regime remained moisture limited, and (3) low WA occurs for the cases where the soil moisture regime remained energy-limited. These results lend support to the hypothesis formulated in Sect. 3.3.

Compared to the response of the above-mentioned coupling metrics in July and August, their change in May and June is considerably smaller in Central Europe (Fig. S16c-e). However, the DTR change is larger over the Iberian Peninsula (Fig. S16c,e). Furthermore, besides the increase in the coupling strength $C_{\theta E}$ over France, increases are also evident across the Northern and Central Iberian Peninsula and the Mediterranean, in contrast to the July-August reduction of $C_{\theta E}$ over the Mediterranean (cf. Figure S16d and Fig. 10b). Similar to July and August, days experiencing an evapotranspiration regime shift in May and June display higher WA (Fig. 11b). Yet, the magnitude is substantially smaller compared to July and August (Fig. 11a). A possible explanation for the lower WA in May-June is that the trajectory of the $EF(\theta)$ data points, as the background warming increases, tends to remain in the upper part of the $EF(\theta)$ dependency, resulting in a higher latent heat flux and thus much smaller contribution from the DTR change. Moreover, the relative share of days that remained energy-limited across all climates is higher for May-June (74.7% in MJ vs. 44.3% in JA in Fig. 11). Thus, the role of soil moisture-temperature coupling in the temperature response to global warming is much larger in late summer.

Finally, to better understand the observed behaviour, we examined the average increments in evaporative fraction ($\Delta EF/\Delta GWL$) and soil moisture ($\Delta\theta/\Delta GWL$) for the three regime-transition cases shown in Fig. 11a. The joint histogram of WA and $\Delta EF/\Delta GWL$ (neglecting non-linearities, for simplicity) for grid points that unambiguously exhibit a given regime-transition case reveals a clear relationship: larger decreases in evaporative fraction are associated with stronger WA (Fig. 12a,b). This behaviour is evident for both the "EL-ML" and "ML-ML" cases, although the magnitude of $\Delta EF/\Delta GWL$ is generally smaller for the latter. The intermittent structure of the distribution in Fig. 12b arises from the asymmetric response of evaporative fraction in dry regions, where only a small number of grid points exhibit increases in soil moisture and, consequently, in evaporative fraction.

We further examined the joint histogram of $\Delta EF/\Delta GWL$ and $\Delta\theta/\Delta GWL$ (Fig. 12d-f). In the case of regime transition (Fig. 12d), soil moisture decreases substantially faster, leading to a pronounced reduction in evaporative fraction and, therefore, strong WA. In contrast, when the initial regime is already moisture-limited (ML-ML, Fig. 12e), soil drying is weaker and accompanied by more moderate changes in evaporative fraction. The shape of the distribution in this case reflects the approximately linear slope of the $EF(\theta)$ relationship in the moisture-limited regime. The EL-EL case (Fig. 12f) corresponds to the flatter portion of the $EF(\theta)$ relationship, where evaporative fraction is relatively insensitive to soil moisture variations, consistent with the plateau observed at high soil moisture values (see example in Fig. S2a). Similar differences in the distributions of $\Delta EF/\Delta GWL$ and $\Delta\theta/\Delta GWL$ for the three regime-transition cases are evident in May-June (Fig. S17).

Although WA exhibits substantial variability for a given increment in evaporative fraction, indicating the influence of additional controlling factors, the magnitude of $\Delta EF/\Delta GWL$ explains the primary differences among the three regime-transition cases.

4 Discussion and conclusions

In this study, we investigated the magnitude and mechanisms behind the response of summer daily maximum 2 m temperatures in the regional storyline simulations of the series of hot and dry summers in the period between 2018 and 2022 in Europe. We used a global-to-regional model chain employing the global coupled model AWI-CM−1.1-MR, with the large-scale horizontal winds spectrally nudged

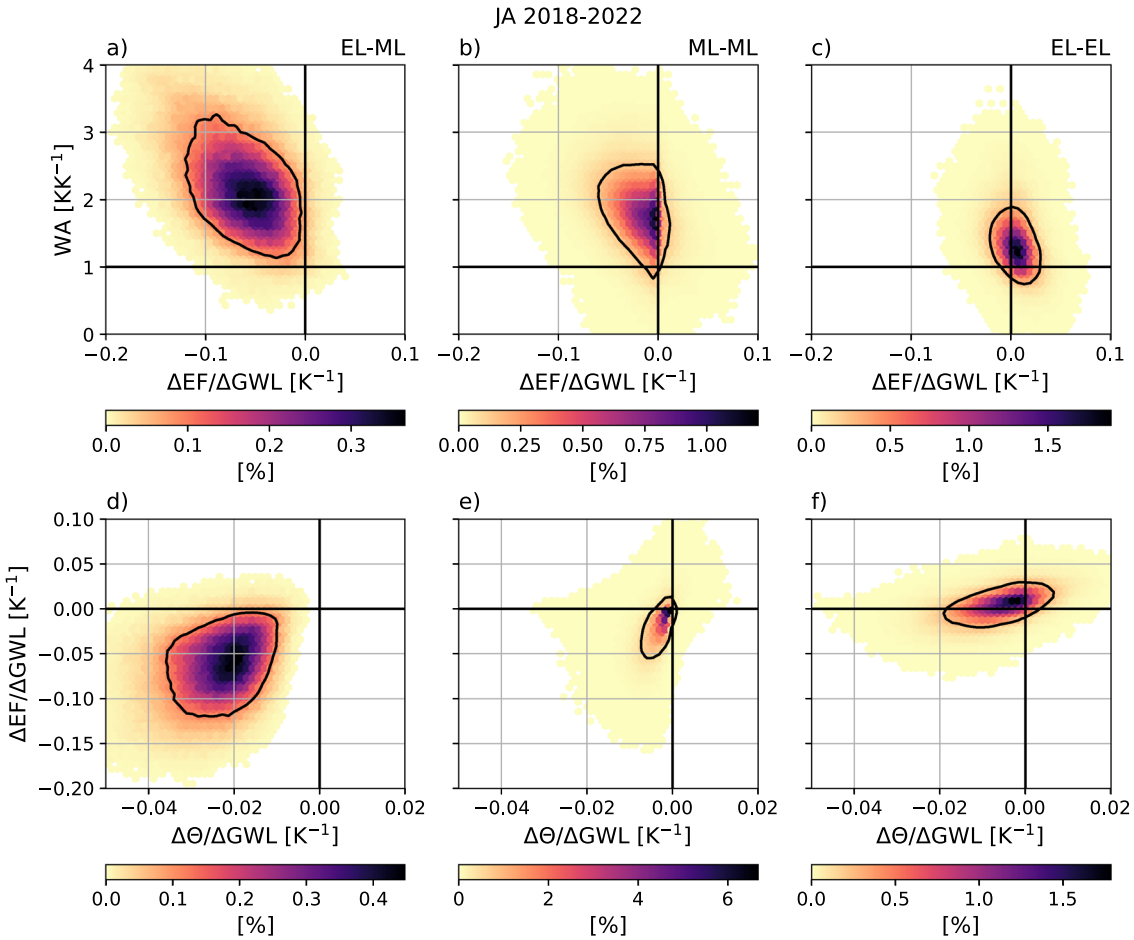

Fig. 12 Hexagonal binning plots of **a-c** warming amplification (WA) versus $\Delta EF/\Delta GWL$ (mean change in evaporative fraction per degree of global warming), and (d-f) $\Delta EF/\Delta GWL$ versus $\Delta\theta/\Delta GWL$ (mean change in soil moisture per degree of global warming), for July-August 2018-2022. Results are shown for grid points within 10°W-30°E and 35°N-65°N where all ensemble members consistently exhibited one of the three evapotranspiration regime transition cases: (a,d) transition from energy-limited to moisture-limited regime (EL-ML), (b,e) no transition within the moisture-limited regime (ML-ML), and (c,f) no transition within the energy-limited regime (EL-EL). Shading indicates the fraction of samples per bin (%). The black contour encloses the region containing 75% of the samples. The bins with fewer than 10 points are not shown

to ERA5 in the free troposphere, and the regional climate model ICON-CLM for further dynamical downscaling of the global storylines to a grid spacing of ∼12 km (Klimiuk et al. 2025).

The results offer the following answers to the research questions initially posed:

1. How well do the model simulations capture the land-atmosphere conditions during 2018-2022? Simulated latent and sensible heat fluxes agree well with both in situ observations and reanalysis products at the evaluation sites, and comparisons over the subregions show good agreement in soil moisture and turbulent heat fluxes where observational references are available. Overall, the consistency in mean states and the high temporal correlations support the realism of the regional ICON simulations over the study area.
2. What are the characteristics of the near-surface temperature response to global warming? We describe the response of the daily maximum near-surface temperature to global warming as warming amplification (WA), the increment of TX per degree of GWL. WA is highly variable in Central Europe. On average, colder summer days exhibit WA close to unity, i.e., they respond to the background warming at the same rate as the global mean temperature. For days with present-day TX between 20 and 36 °C, WA increases with higher TX, and the range of possible WA values is large. WA tends to stabilize above this temperature range and remains near 2.0 KK^{-1} for the highest present-day maximum temperatures. A strong variability of WA at moderately high maximum temperatures implies that two days with a similar maximum temperature can respond to the background warming with considerably different amplification, ranging

between 0 and 4 KK^{-1}. Separating the response by months revealed that WA in early (late) summer tends to be lower (higher), and most of the events with higher WA occurred in August.

3. How does the evapotranspiration regime respond to climate change in the nudged regional storyline simulations? According to our regional storyline simulations, the evapotranspiration regimes that are dominant for each particular month redistribute with increased background warming. For Central Europe, May and June tend to stay in the energy-limited part of the $EF(\theta)$ dependency in all climates. In contrast, July, August, and September become more moisture-limited with higher global warming levels. This change is seen as a movement of data points further towards the steeper slope of the $EF(\theta)$ dependency as soil moisture decreases below a critical value θ_{crit}. In more arid regions, such as the Central and Southern Iberian Peninsula, we find little to no redistribution of evapotranspiration regimes: the prevailing regime remains moisture-limited throughout the entire summer season in each simulated climate.
4. Is there a connection between the evapotranspiration regime change and the magnitude of the daily maximum near-surface temperature response? Our findings reveal that the WA magnitude can at least partially be explained by the changes in the relationship between soil moisture and evapotranspiration with increasing background warming. According to our regional storyline simulations, the highest WA of daily maximum temperature is often accompanied by a shift from an energy-limited to a moisture-limited evapotranspiration regime (see Fig. 11). In this case, WA on hotter days approaches and exceeds 3 KK^{-1}. If an event was already amplified by strong soil moisture-temperature coupling in the present-day climate, its intensity tends to show a slightly weaker WA, although WA still reaches 2 KK^{-1}. For events in which the evapotranspiration regime remains energy-limited in all climates, WA tends to be smaller than 2 KK^{-1}. In that case, the evapotranspiration stays unconstrained by soil moisture, implying little to no change in the soil moisture-temperature coupling strength with increased background warming. We conclude that WA is largely attributable to the sensitivity of surface energy partitioning to soil moisture, reflected in an increase in TX as evaporative fraction decreases along the slope of the $EF(\theta)$ relationship. Moreover, events undergoing a regime transition exhibit substantially stronger soil drying, whereas drying remains limited in the case of ML-ML events (Fig. 12). This suggests that one mechanism behind the lower WA of already dry heatwaves is the reduced potential for further soil drying. Although at the daily timescale the moisture-limited regime enhances heat extremes, at the climatological scale this effect can be interpreted as a limiting feedback: evapotranspiration is already suppressed prior to and during the event at higher GWLs, which constrains additional soil drying and reduces the corresponding increase in sensible heating. In contrast, the strongest WA occurs in EL-ML transition events, where soils remain susceptible to drying and large reductions in evaporative fraction can occur as warming progresses.

The redistribution of evapotranspiration regimes under increased background warming leads to a larger fraction of Europe exhibiting enhanced soil moisture-temperature coupling. Having shown that the range of reachable TX in such areas increases much faster than in regions already in the moisture-limited regime, we conclude that the areas with a strong coupling will expand considerably in Europe. Moreover, the increase in moisture-limited days in May-June over the Mediterranean (Fig. S15) suggests an earlier seasonal onset of highly coupled conditions in this region. These findings are consistent with Dirmeyer et al. (2013) and Hsu and Dirmeyer (2023a), who reported that regions of strong coupling extend beyond their historical boundaries and that evapotranspiration regimes undergo a seasonal redistribution in warmer climates, based on CMIP5 and CMIP6 simulations.

Furthermore, the increase in land-atmosphere coupling strength over Central and Eastern Europe and its decrease over the Mediterranean, shown in Fig. 10b, is consistent with Seneviratne et al. (2006). Their results indicated a northward shift of climatic zones, leading to increased interannual summer temperature variability in Central and Eastern Europe, largely driven by the activation of land-atmosphere coupling under elevated greenhouse gas concentrations.

Notably, Zhang and Boos (2023) found a similar increase rate for the maximum reachable air temperatures over mid-latitude land (2 KK^{-1}). Within the convective-instability framework, they demonstrated that the upper limit for near-surface temperature increase is approximately twice the rate of air temperature change at 500 hPa, which itself closely tracks the rate of global mean surface air temperature rise. Furthermore, Zhang and Boos (2023) identified the surface air specific humidity as a key determinant for this upper bound and indicated that it depends on multiple processes of land-atmosphere interaction, as well as the advection of moisture from the oceans. They suggest that regions experiencing drying on the hottest days will likely see a more rapid increase in annual maximum near-surface temperatures. In the current study, we observe a stronger increase in areas that enter a moisture-limited regime in the future climate; however, the response of surface air specific humidity to the background warming is required before drawing

conclusions about its connection with the WA presented in this work.

The wide range of possible magnitudes of WA for the moderately high maximum temperatures (see Fig. 6) may be traced back to several interdependent factors. As only the large-scale circulation in the free troposphere was nudged to reanalysis data in our simulations, it is still possible that the smaller-scale changes in circulation lead to variations in the local air mass characteristics. This may result in either an intensification or a weakening of heat events. Moreover, as discussed in Miralles et al. (2019), advection of hot and dry air from the upstream regions may cause the propagation of heatwaves and droughts downstream. Nevertheless, disregarding the reasons for soil desiccation, our results provide clear evidence that the highest WA is usually accompanied by a transition towards the moisture-limited evapotranspiration regime.

As discussed in Sect. 2.2, we assume in this analysis that θ_{crit} is stationary with increasing GWL, although we identified a weak decrease in θ_{crit} in our simulations (Fig. S2c). Non-stationarity in θ_{crit} is physically plausible, as it depends not only on soil characteristics but also on the local surface energy balance, and Hsu and Dirmeyer (2023b) showed that its behaviour may differ among GCMs, with implications for the hydrological cycle. However, over Europe, only a few models exhibit any significant changes in θ_{crit} (Hsu and Dirmeyer 2023b). We therefore retain the assumption of stationarity in the present analysis. Moreover, before attributing changes in θ_{crit} to physical processes, we must first exclude the influence of the calculation method; this will be addressed in future work.

In this study, we investigated the relationship between evapotranspiration and soil moisture and deliberately focused on the qualitative assessment of its changes with increasing background warming. This provides new insights into the mechanisms behind the soil moisture-temperature coupling and its response to background warming. The magnitude of this coupling can be further assessed by, e.g., computing the actual slope of the $EF(\theta)$ and $T(EF)$ relationships (e.g., Schwingshackl et al. 2018). Another metric to quantify the land-atmosphere coupling strength was introduced by Miralles et al. (2012); it is expressed as the difference between the correlation of temperature with sensible heat flux and the correlation of temperature with the potential sensible heat flux (computed with potential evapotranspiration), reflecting the contribution of sensible heat flux to the temperature variability. The application of the coupling metrics to event-based storyline simulations would provide additional insights into the role of land-atmosphere coupling on the response of summer near-surface temperature to global warming.

We highlight the value of the evapotranspiration regime framework in both analyzing the characteristics of present-day heatwaves and drawing conclusions about how heatwaves may evolve in the future. By gaining a better understanding of the processes behind the intensification of heatwaves through the use of this framework on the storyline simulations, we can estimate peak temperatures that can be expected in each particular region with more confidence. Nevertheless, it is worth noting that the actual response of regional climate systems to global warming will also depend on dynamical changes, including the influence of local land-atmosphere interactions on global circulation, which are intentionally suppressed in the nudged experiments. By constraining the large-scale atmospheric circulation, the storyline approach enables a targeted investigation of soil drying and surface energy partitioning. It should therefore be viewed as complementary to free-running simulations, providing insight into thermodynamic sensitivities under identical circulation conditions rather than a complete projection of future climate.

The evapotranspiration regime framework has been widely applied to global free-running simulations, reanalyses, and observations (Schwingshackl et al. 2017, 2018; Haghighi et al. 2018; Feldman et al. 2019; Dirmeyer et al. 2021). The increasing availability of high-resolution regional climate simulations provides new opportunities for process-based analyses at regional scales, with the use of simulations such as those enabled by CORDEX (Jacob et al. 2014; Kotlarski et al. 2014; Knist et al. 2017; Jacob et al. 2020). The insights provided by this research may facilitate the interpretation of projected changes, in particular, disentangling of purely thermodynamic effects from the complex interplay of climate feedbacks on global circulation.

The main conclusion of our study is that peak temperatures of dry heat extremes would be amplified by about 2 K per degree of global warming. Furthermore, as previously shown in Hundhausen et al. (2023) and Klimiuk et al. (2025), the stronger increase of daily maximum 2 m-temperatures in July and August implies an increase in the occurrence, duration, and extent of heatwaves in late summer over Central Europe. Here, we partially attributed this growth to the decline of soil moisture below the critical value in warmer climates. This decline activates the soil moisture-temperature coupling through the limitation of evapotranspiration, leading to WA reaching 3 KK^{-1}. In contrast, evapotranspiration in May and June tends to remain energy-limited as the background warming increases, and the coupling between soil moisture and evapotranspiration is less likely to have a strong influence on the heatwave intensities for that period. This information thus provides a basis for targeted adaptation strategies, especially those aimed at mitigating late-summer heatwave risks under continued warming.

Supplementary Information The online version contains supplementary material available at https://doi.org/10.1007/s00382-026-08205-0.

Acknowledgements The authors thank the German Climate Computing Center (DKRZ), Hamburg, for providing computing and storage resources under project nos. 105 and 1264. The authors acknowledge Haojin Zhao and Dr. Bibi Naz from Forschungszentrum Juelich, Germany, for providing the post-processed SMAP and TERENO datasets. The authors thank Jan Streffing from Alfred Wegener Institute, Bremerhaven, Germany, for providing the performance indices of AWI-CM−1.1-MR. The authors thank the Helmholtz Research Field Earth & Environment for funding this research within the Innopool SCENIC and ACTUATE projects. Joaquim G. Pinto thanks the AXA research fund for support. We acknowledge the E-OBS dataset from the EU-FP6 project UERRA (https://www.uerra.eu) and the Copernicus Climate Change Service, and the data providers in the ECA&D project (https://www.ecad.eu). We thank Paul Dirmeyer and two anonymous reviewers for their valuable feedback that helped us to considerably improve the manuscript.

Author Contributions Tatiana Klimiuk, Patrick Ludwig, and Joaquim G. Pinto conceived and designed the study. Antonio Sanchez-Benitez computed the global AWI-CM1 simulations and provided the data and necessary instructions. Patrick Ludwig took care of the pre-processing of the input data for ICON. Tatiana Klimiuk performed the ICON simulations, performed the literature review and data analysis, prepared the figures, and wrote the initial draft of the article. All authors discussed the results and contributed to the paper revisions.

Funding Open Access funding enabled and organized by Projekt DEAL. This research has been supported by funding from the Helmholtz research field "Earth & Environment" for the Innovation Pool project SCENIC and subsequently the Innovation Pool project ACTUATE. Joaquim G. Pinto received support from the AXA Research Fund.

Data Availability The ICON model has been available as open-source code since January 2024 at https://gitlab.dkrz.de/icon/icon-model. The runtime environment SPICE v2.0 is available online at https://doi.org/10.5281/zenodo.6838984 (Rockel and Geyer 2022). The storyline simulations are stored on the supercomputer Levante at the German Climate Computing Center (DKRZ), Hamburg, and can be made available upon request. ERA5 and ERA5-Land data can be downloaded from the Copernicus Climate Change Service (C3S) Climate Data Store (https://doi.org/10.24381/cds.adbb2d47 and https://cds.climate.copernicus.eu/datasets/reanalysis-era5-land?-timeseries, respectively) and can be accessed at DKRZ by users of the Levante high-performance computing (HPC) system. The E-OBS dataset can be accessed via the website of the European Climate Assessment & Dataset project (https://surfobs.climate.copernicus.eu/dataaccess/access_eobs.php#datafiles). The ICOS ecosystem data for the DE-RuS and FR-Fon stations were downloaded from the ICOS Carbon portal, https://doi.org/10.18160/S6HM-CP8Q (Icos Ri et al. 2025). The TERENO datasets for soil moisture and latent heat flux were provided by Dr. Bibi Naz, Forschungszentrum Juelich; the original dataset can be downloaded at: https://ddp.tereno.net/ddp/.

Declarations

Conflict of interest The authors have no relevant financial or non-financial interests to disclose.

References

Aalbers EE, Meijgaard E, Lenderink G, Vries H, Hurk BJJM (2023) The 2018 west-central European drought projected in a warmer climate: how much drier can it get? Nat Hazards Earth Syst Sci 23(5):1921–1946. https://doi.org/10.5194/nhess-23-1921-2023

Budyko MI, Berlyand TG, Yefimova NA, Zubenok LI, Strokina LA (1980) Heat balance of the Earth. NTRS Author Affiliations: NASA Headquarters NTRS Report/Patent Number: NASA-TM-75826 NTRS Document ID: 19810004876 NTRS Research Center: Legacy CDMS (CDMS) . https://ntrs.nasa.gov/citations/19810004876 Accessed 2025-09-11

Benson DO, Dirmeyer PA (2021) Characterizing the Relationship between Temperature and Soil Moisture Extremes and Their Role in the Exacerbation of Heat Waves over the Contiguous United States. J Clim 34(6):2175–2187. https://doi.org/10.1175/JCLI-D-20-0440.1

Bateni SM, Entekhabi D (2012) Relative efficiency of land surface energy balance components. Water Resour Res. https://doi.org/10.1029/2011WR011357

Barriopedro D, García-Herrera R, Ordóñez C, Miralles DG, Salcedo-Sanz S (2023) Heat waves: physical understanding and scientific challenges. Rev Geophys 61(2):01–10. https://doi.org/10.1029/2022RG000780

Baldissera Pacchetti M, Coulter L, Dessai S, Shepherd TG, Sillmann J, Van Den Hurk B (2024) Varieties of approaches to constructing physical climate storylines: a review. WIREs Clim Change 15(2):869. https://doi.org/10.1002/wcc.869

Bevacqua E, Rakovec O, Schumacher DL, Kumar R, Thober S, Samaniego L, Seneviratne SI, Zscheischler J (2024) Direct and lagged climate change effects intensified the 2022 European drought. Nat Geosci 17(11):1100–1107. https://doi.org/10.1038/s41561-024-01559-2

Baulenas E, Versteeg G, Terrado M, Mindlin J, Bojovic D (2023) Assembling the climate story: use of storyline approaches in climate-related science. Global Chall 7(7):2200183. https://doi.org/10.1002/gch2.202200183

Cattiaux J, Douville H, Schoetter R, Parey S, Yiou P (2015) Projected increase in diurnal and interdiurnal variations of European summer temperatures. Geophys Res Lett 42(3):899–907. https://doi.org/10.1002/2014GL062531

Copernicus Climate Change Service (2024) Monitoring European climate using surface observations | Copernicus Climate Change Service . https://surfobs.climate.copernicus.eu/ Accessed 2025-09-10

Cornes RC, Schrier G, Besselaar EJM, Jones PD (2018) An ensemble version of the E-OBS temperature and precipitation data sets. J Geophys Res Atmos 123(17):9391–9409. https://doi.org/10.1029/2017JD028200

Dong J, Akbar R, Short Gianotti DJ, Feldman AF, Crow WT, Entekhabi D (2022) Can surface soil moisture information identify evapotranspiration regime transitions? Geophys Res Lett 49(7):2021–097697. https://doi.org/10.1029/2021GL097697

Dirmeyer PA, Balsamo G, Blyth EM, Morrison R, Cooper HM (2021) Land-atmosphere interactions exacerbated the drought and heatwave over Northern Europe during summer 2018. AGU Adv. https://doi.org/10.1029/2020AV000283

Doms G, Forstner J, Heise E, Reinhardt T, Ritter B, Schrodin R, Schulz J-P, Vogel G (2021) A description of the nonhydrostatic regional COSMO-Model. Consort Small-Scale Model. https://doi.org/10.5676/DWD_pub/nwv/cosmo-doc_6.00_II

Dickinson RE (1984) Modeling Evapotranspiration for Three-Dimensional Global Climate Models, 58–72. American Geophysical Union (AGU), Washington, D.C. .https://doi.org/10.1029/GM029p0058

Dirmeyer PA (2011) The terrestrial segment of soil moisture-climate coupling. Geophys Res Lett. https://doi.org/10.1029/2011GL048268

Dirmeyer PA, Jin Y, Singh B, Yan X (2013) Evolving land-atmosphere interactions over North America from CMIP5 simulations. J Clim 26(19):7313–7327. https://doi.org/10.1175/JCLI-D-12-00454.1

Dai A, Trenberth KE, Karl TR (1999) Effects of Clouds, Soil Moisture, Precipitation, and Water Vapor on Diurnal Temperature Range. J Clim 12(8):2451–2473. https://doi.org/10.1175/1520-0442(1999)012%26lt;2451:EOCSMP%26gt;2.0.CO;2 (**Publisher: American Meteorological Society**)

Vries H, Lenderink G, Meijgaard E, Ulft B, Rooy W (2024) Western Europe's extreme July 2019 heatwave in a warmer world. Environ Res Clim 3(3):035005. https://doi.org/10.1088/2752-5295/ad519f

Entekhabi D, Das N, Njoku E, Johnson J, Shi J (2016) SMAP L3 Radar/Radiometer Global Daily 9 km EASE-Grid Soil Moisture, Version 3. NASA Nat Snow Ice Data Center Distrib Active Arch Center. https://doi.org/10.5067/7KKNQ5UURM2W. (http://nsidc.org/data/SPL3SMAP/versions/3)

Fu Z, Ciais P, Wigneron J-P, Gentine P, Feldman AF, Makowski D, Viovy N, Kemanian AR, Goll DS, Stoy PC, Prentice IC, Yakir D, Liu L, Ma H, Li X, Huang Y, Yu K, Zhu P, Li X, Zhu Z, Lian J, Smith WK (2024) Global critical soil moisture thresholds of plant water stress. Nat Commun 15:4826. https://doi.org/10.1038/s41467-024-49244-7

Feser F, Garderen Lv, Hansen F (2024) The Summer Heatwave 2022 over Western Europe: An Attribution to Anthropogenic Climate Change. Bull Am Meteor Soc 105(11):2175–2179. https://doi.org/10.1175/BAMS-D-24-0017.1

Fischer EM, Schär C (2010) Consistent geographical patterns of changes in high-impact European heatwaves. Nat Geosci 3(6):398–403. https://doi.org/10.1038/ngeo866

Feser F, Shepherd TG (2025) The concept of spectrally nudged storylines for extreme event attribution. Commun Earth Environ 6(1):677. https://doi.org/10.1038/s43247-025-02659-6

Feldman AF, Short Gianotti DJ, Trigo IF, Salvucci GD, Entekhabi D (2019) Satellite-based assessment of land surface energy partitioning-soil moisture relationships and effects of confounding variables. Water Resour Res 55(12):10657–10677. https://doi.org/10.1029/2019WR025874

Fischer EM, Seneviratne SI, Lüthi D, Schär C (2007) Contribution of land-atmosphere coupling to recent European summer heat waves. Geophys Res Lett. https://doi.org/10.1029/2006GL029068

Gevaert AI, Miralles DG, Jeu, RaM, Schellekens J, Dolman AJ (2018) Soil Moisture-Temperature Coupling in a Set of Land Surface Models. Journal of Geophysical Research Atmospheres 123(3):1481–1498. https://doi.org/10.1002/2017JD027346

Hersbach H, Bell B, Berrisford P, Hirahara S, Horányi A, Muñoz-Sabater J, Nicolas J, Peubey C, Radu R, Schepers D, Simmons A, Soci C, Abdalla S, Abellan X, Balsamo G, Bechtold P, Biavati G, Bidlot J, Bonavita M, De Chiara G, Dahlgren P, Dee D, Diamantakis M, Dragani R, Flemming J, Forbes R, Fuentes M, Geer A, Haimberger L, Healy S, Hogan RJ, Hólm E, Janisková M, Keeley S, Laloyaux P, Lopez P, Lupu C, Radnoti G, Rosnay P, Rozum I, Vamborg F, Villaume S, Thépaut J-N (2020) The ERA5 global reanalysis. Q J R Meteorol Soc 146(730):1999–2049. https://doi.org/10.1002/qj.3803

Hsu H, Dirmeyer PA (2023) Soil moisture-evaporation coupling shifts into new gears under increasing CO2. Nat Commun 14(1):1162. https://doi.org/10.1038/s41467-023-36794-5

Hsu H, Dirmeyer PA (2023) Uncertainty in projected critical soil moisture values in cmip6 affects the interpretation of a more moisture-limited world. Earth's Future 11(6):2023–003511. https://doi.org/10.1029/2023EF003511

Hsu H, Dirmeyer PA, Seo E (2024) Exploring the Mechanisms of the Soil Moisture-Air Temperature Hypersensitive Coupling Regime. Water Resour Res 60(7):2023–036490. https://agupubs.onlinelibrary.wiley.com/doi/pdf/10.1029/2023WR036490. https://doi.org/10.1029/2023WR036490

Huguenin MF, Fischer EM, Kotlarski S, Scherrer SC, Schwierz C, Knutti R (2020) Lack of change in the projected frequency and persistence of atmospheric circulation types over Central Europe. Geophys Res Lett 47(9):2019–086132. https://doi.org/10.1029/2019GL086132

Hundhausen M, Feldmann H, Laube N, Pinto JG (2023) Future heat extremes and impacts in a convection-permitting climate ensemble over Germany. Nat Hazards Earth Syst Sci 23(8):2873–2893. https://doi.org/10.5194/nhess-23-2873-2023

Haghighi E, Short Gianotti DJ, Akbar R, Salvucci GD, Entekhabi D (2018) Soil and atmospheric controls on the land surface energy balance: a generalized framework for distinguishing moisture-limited and energy-limited evaporation regimes. Water Resour Res 54(3):1831–1851. https://doi.org/10.1002/2017WR021729

ICOS RI, Aalto J, Aalto P, Aaltonen H, Aiguier T, Akubia J, Ala-Könni J, Alivernini A, Alonso L, Aluome C, Andersson T, Arriga N, Aurela M, BRECHET L, Baab F, Back J, Bagheri S, Baltes U, Baneschi I, Barral H, Barten S, Bastos Campos F, Baur T, Bauters M, Bazot S, Beauclair P, Becker N, Behrens N, Belelli Marchesini L, Bergström G, Bernhofer C, Berveiller D, Biermann T, Bignotti L, Biron R, Bloor J (2025) Ecosystem final quality (L2) product in ETC-Archive format - release 2025-1. ICOS ERIC – Carbon Portal. Medium: Arbitrary ZIP archive,ICOS ETC half-hourly product CSV Version Number: 1.0 . https://doi.org/10.18160/S6HM-CP8Q . https://meta.icos-cp.eu/collections/1-HA2r4l5QUjAgQr5CCEfJe3 Accessed 2025-08-25

Jacob D, Petersen J, Eggert B, Alias A, Christensen OB, Bouwer LM, Braun A, Colette A, Déqué M, Georgievski G, Georgopoulou E, Gobiet A, Menut L, Nikulin G, Haensler A, Hempelmann N, Jones C, Keuler K, Kovats S, Kröner N, Kotlarski S, Kriegsmann A, Martin E, Meijgaard E, Moseley C, Pfeifer S, Preuschmann S, Radermacher C, Radtke K, Rechid D, Rounsevell M, Samuelsson P, Somot S, Soussana J-F, Teichmann C, Valentini R, Vautard R, Weber B, Yiou P (2014) EURO-CORDEX: new high-resolution climate change projections for European impact research. Reg Environ Change 14(2):563–578. https://doi.org/10.1007/s10113-013-0499-2

Jacob D, Teichmann C, Sobolowski S, Katragkou E, Anders I, Belda M, Benestad R, Boberg F, Buonomo E, Cardoso RM, Casanueva A, Christensen OB, Christensen JH, Coppola E, De Cruz L, Davin EL, Dobler A, Domínguez M, Fealy R, Fernandez J, Gaertner MA, García-Díez M, Giorgi F, Gobiet A, Goergen K, Gómez-Navarro JJ, Alemán JJG, Gutiérrez C, Gutiérrez JM, Güttler I, Haensler A, Halenka T, Jerez S, Jiménez-Guerrero P, Jones RG, Keuler K, Kjellström E, Knist S, Kotlarski S, Maraun D, Meijgaard E, Mercogliano P, Montávez JP, Navarra A, Nikulin G,

Noblet-Ducoudré N, Panitz H-J, Pfeifer S, Piazza M, Pichelli E, Pietikäinen J-P, Prein AF, Preuschmann S, Rechid D, Rockel B, Romera R, Sánchez E, Sieck K, Soares PMM, Somot S, Srnec L, Sørland SL, Termonia P, Truhetz H, Vautard R, Warrach-Sagi K, Wulfmeyer V (2020) Regional climate downscaling over Europe: perspectives from the EURO-CORDEX community. Reg Environ Change 20(2):51. https://doi.org/10.1007/s10113-020-01606-9

Knutzen F, Averbeck P, Barrasso C, Bouwer LM, Gardiner B, Grünzweig JM, Hänel S, Haustein K, Johannessen MR, Kollet S, Müller MM, Pietikäinen J-P, Pietras-Couffignal K, Pinto JG, Rechid D, Rousi E, Russo A, Suarez-Gutierrez L, Veit S, Wendler J, Xoplaki E, Gliksman D (2025) Impacts on and damage to European forests from the 2018–2022 heat and drought events. Nat Hazards Earth Syst Sci 25(1):77–117. https://doi.org/10.5194/nhess-25-77-2025

Koster RD, Feldman AF, Holmes TRH, Anderson MC, Crow WT, Hain C (2024) Estimating Hydrological Regimes from Observational Soil Moisture, Evapotranspiration, and Air Temperature Data. J Hydrometeorol 25(3):495–513. https://doi.org/10.1175/JHM-D-23-0140.1

Knist S, Goergen K, Buonomo E, Christensen OB, Colette A, Cardoso RM, Fealy R, Fernández J, García-Díez M, Jacob D, Kartsios S, Katragkou E, Keuler K, Mayer S, Meijgaard E, Nikulin G, Soares PMM, Sobolowski S, Szepszo G, Teichmann C, Vautard R, Warrach-Sagi K, Wulfmeyer V, Simmer C (2017) Land-atmosphere coupling in EURO-CORDEX evaluation experiments. J Geophys Res Atmos 122(1):79–103. https://doi.org/10.1002/2016JD025476

Kotlarski S, Keuler K, Christensen OB, Colette A, Déqué M, Gobiet A, Goergen K, Jacob D, Lüthi D, Meijgaard E, Nikulin G, Schär C, Teichmann C, Vautard R, Warrach-Sagi K, Wulfmeyer V (2014) Regional climate modeling on European scales: a joint standard evaluation of the EURO-CORDEX RCM ensemble. Geosci Model Dev 7(4):1297–1333. https://doi.org/10.5194/gmd-7-1297-2014

Klimiuk T, Ludwig P, Sanchez-Benitez A, Goessling HF, Braesicke P, Pinto JG (2025) The European summer heatwave of 2019 – a regional storyline perspective. Earth Syst Dyn 16(1):239–255. https://doi.org/10.5194/esd-16-239-2025

Kautz L-A, Martius O, Pfahl S, Pinto JG, Ramos AM, Sousa PM, Woollings T (2022) Atmospheric blocking and weather extremes over the Euro-Atlantic sector – a review. Weather Climate Dyn 3(1):305–336. https://doi.org/10.5194/wcd-3-305-2022

Koster RD, Schubert SD, Suarez MJ (2009) Analyzing the concurrence of meteorological droughts and warm periods, with implications for the determination of evaporative regime. J Clim 22(12):3331–3341. https://doi.org/10.1175/2008JCLI2718.1

Lemus-Canovas M, Gonzalez-Herrero S, Trapero L, Albalat A, Insua-Costa D, Senande-Rivera M, Miguez-Macho G (2025) Exploring the interplay between observed warming, atmospheric circulation, and soil–atmosphere feedbacks on heatwaves in a temperate mountain region. Nat Hazards Earth Syst Sci 25(7):2503–2518. https://doi.org/10.5194/nhess-25-2503-2025

Ludwig P, Ehmele F, Franca MJ, Mohr S, Caldas-Alvarez A, Daniell JE, Ehret U, Feldmann H, Hundhausen M, Knippertz P, Küpfer K, Kunz M, Mühr B, Pinto JG, Quinting J, Schäfer AM, Seidel F, Wisotzky C (2023) A multi-disciplinary analysis of the exceptional flood event of July 2021 in central europe – part 2: Historical context and relation to climate change. Nat Hazards Earth Syst Sci 23(4):1287–1311. https://doi.org/10.5194/nhess-23-1287-2023

Miralles DG, Bonte O, Koppa A, Baez-Villanueva OM, Tronquo E, Zhong F, Beck HE, Hulsman P, Dorigo W, Verhoest NEC, Haghdoost, S (2025) GLEAM4: global land evaporation and soil moisture dataset at 0.1° resolution from, (1980) to near present. Scientific Data 12(1):416. https://doi.org/10.1038/s41597-025-04610-y

Mohr S, Ehret U, Kunz M, Ludwig P, Caldas-Alvarez A, Daniell JE, Ehmele F, Feldmann H, Franca MJ, Gattke C, Hundhausen M, Knippertz P, Kuepfer K, Muehr B, Pinto JG, Quinting J, Schäfer AM, Scheibel M, Seidel F, Wisotzky C (2023) A multi-disciplinary analysis of the exceptional flood event of July 2021 in central Europe. Part 1: Event description and analysis. Nat Hazards Earth Syst Sci 23:525–551. https://doi.org/10.5194/nhess-23-525-2023

Miralles DG, Gentine P, Seneviratne SI, Teuling AJ (2019) Land–atmospheric feedbacks during droughts and heatwaves: state of the science and current challenges. Ann N Y Acad Sci 1436(1):19–35. https://doi.org/10.1111/nyas.13912

Miralles DG, Holmes TRH, De Jeu RaM, Gash JH, Meesters AGCA, Dolman AJ (2011) Global land-surface evaporation estimated from satellite-based observations. Hydrol Earth Syst Sci 15(2):453–469. https://doi.org/10.5194/hess-15-453-2011

Muñoz-Sabater J, Dutra E, Agustí-Panareda A, Albergel C, Arduini G, Balsamo G, Boussetta S, Choulga M, Harrigan S, Hersbach H, Martens B, Miralles DG, Piles M, Rodríguez-Fernández NJ, Zsoter E, Buontempo C, Thépaut J-N (2021) ERA5-Land: a state-of-the-art global reanalysis dataset for land applications. Earth Syst Sci Data 13(9):4349–4383. https://doi.org/10.5194/essd-13-4349-2021

Meehl GA, Tebaldi C (2004) More intense, more frequent, and longer lasting heat waves in the 21st century. Science 305(5686):994–997. https://doi.org/10.1126/science.1098704

Miralles DG, Teuling AJ, Heerwaarden CC, Arellano J (2014) Mega-heatwave temperatures due to combined soil desiccation and atmospheric heat accumulation. Nat Geosci 7(5):345–349. https://doi.org/10.1038/ngeo2141

Miralles DG, Berg MJ, Teuling AJ, Jeu RaM (2012) Soil moisture-temperature coupling: A multiscale observational analysis. Geophys Res Lett. **39**(21) https://doi.org/10.1029/2012GL053703

Pithan F, Athanase M, Dahlke S, Sánchez-Benítez A, Shupe MD, Sledd A, Streffing J, Svensson G, Jung T (2023) Nudging allows direct evaluation of coupled climate models with in situ observations: a case study from the MOSAiC expedition. Geosci Model Dev 16(7):1857–1873. https://doi.org/10.5194/gmd-16-1857-2023

Perkins SE, Alexander LV, Nairn JR (2012) Increasing frequency, intensity and duration of observed global heatwaves and warm spells. Geophys Res Lett. https://doi.org/10.1029/2012GL053361

Paul S, Feldman AF, Karthikeyan L (2024) Are rootzone soil moisture dynamics and thresholds associated with surface layer? Environ Res Lett 20(1):014037. https://doi.org/10.1088/1748-9326/ad9293

Panwar A, Kleidon A, Renner M (2019) Do surface and air temperatures contain similar imprints of evaporative conditions? Geophys Res Lett 46(7):3802–3809. https://doi.org/10.1029/2019GL082248

Pham TV, Steger C, Rockel B, Keuler K, Kirchner I, Mertens M, Rieger D, Zängl G, Früh B (2021) ICON in Climate Limited-area Mode (ICON release version 2.6.1): a new regional climate model. Geosci Model Dev 14(2):985–1005 https://doi.org/10.5194/gmd-14-985-2021 . Publisher: Copernicus GmbH

Peng L, Zeng Z, Wei Z, Chen A, Wood EF, Sheffield J (2019) Determinants of the ratio of actual to potential evapotranspiration. Glob Change Biol 25(4):1326–1343. https://doi.org/10.1111/gcb.14577

Qiu J, Crow WT, Nearing GS (2016) The impact of vertical measurement depth on the information content of soil moisture for latent heat flux estimation. J Hydrometeorol 17(9):2419–2430. https://doi.org/10.1175/JHM-D-16-0044.1

Rousi E, Fink AH, Andersen LS, Becker FN, Beobide-Arsuaga G, Breil M, Cozzi G, Heinke J, Jach L, Niermann D, Petrovic D, Richling A, Riebold J, Steidl S, Suarez-Gutierrez L, Tradowsky JS,

Coumou D, Düsterhus A, Ellsäßer F, Fragkoulidis G, Gliksman D, Handorf D, Haustein K, Kornhuber K, Kunstmann H, Pinto JG, Warrach-Sagi K, Xoplaki E (2023) The extremely hot and dry 2018 summer in central and northern Europe from a multi-faceted weather and climate perspective. Nat Hazards Earth Syst Sci 23(5):1699–1718. https://doi.org/10.5194/nhess-23-1699-2023

Rockel B, Geyer B (2022) SPICE (Starter Package for ICON-CLM Experiments). Zenodo. https://doi.org/10.5281/zenodo.6838984. https://zenodo.org/records/6838984 Accessed 2024-05-06

Rakovec O, Samaniego L, Hari V, Markonis Y, Moravec V, Thober S, Hanel M, Kumar R (2022) The 2018–2020 multi-year drought sets a new Benchmark in Europe. Earth's Future 10(3):2021–002394. https://doi.org/10.1029/2021EF002394 (https://agupubs.onlinelibrary.wiley.com/doi/pdf/10.1029/2021EF002394)

Shepherd TG, Boyd E, Calel RA, Chapman SC, Dessai S, Dima-West IM, Fowler HJ, James R, Maraun D, Martius O, Senior CA, Sobel AH, Stainforth DA, Tett SFB, Trenberth KE, Hurk BJJM, Watkins NW, Wilby RL, Zenghelis DA (2018) Storylines: an alternative approach to representing uncertainty in physical aspects of climate change. Clim Change 151(3):555–571. https://doi.org/10.1007/s10584-018-2317-9

Sousa PM, Barriopedro D, García-Herrera R, Ordóñez C, Soares PMM, Trigo RM (2020) Distinct influences of large-scale circulation and regional feedbacks in two exceptional 2019 European heatwaves. Commun Earth Environ 1(1):1–13. https://doi.org/10.1038/s43247-020-00048-9

Sousa PM, Barriopedro D, García-Herrera R, Woollings T, Trigo RM (2021) A new combined detection algorithm for blocking and subtropical ridges. J Clim 34(18):7735–7758. https://doi.org/10.1175/JCLI-D-20-0658.1

Sánchez-Benítez A, Goessling H, Pithan F, Semmler T, Jung T (2022) The July 2019 European heat wave in a warmer climate: storyline scenarios with a coupled model using spectral nudging. J Clim 35(8):2373–2390. https://doi.org/10.1175/JCLI-D-21-0573.1

Seneviratne SI, Corti T, Davin EL, Hirschi M, Jaeger EB, Lehner I, Orlowsky B, Teuling AJ (2010) Investigating soil moisture-climate interactions in a changing climate: a review. Earth Sci Rev 99:125–161. https://doi.org/10.1016/j.earscirev.2010.02.004

Santanello JA, Dirmeyer PA, Ferguson CR, Findell KL, Tawfik AB, Berg A, Ek M, Gentine P, Guillod BP, Heerwaarden Cv, Roundy J, Wulfmeyer V (2018) Land-Atmosphere Interactions: The LoCo Perspective. Bull Am Meteor Soc 99(6):1253–1272. https://doi.org/10.1175/BAMS-D-17-0001.1

Semmler T, Danilov S, Gierz P, Goessling HF, Hegewald J, Hinrichs C, Koldunov N, Khosravi N, Mu L, Rackow T, Sein DV, Sidorenko D, Wang Q, Jung T (2020) Simulations for CMIP6 With the AWI climate model AWI-CM-1-1. J Adv Model Earth Syst 12(9):2019–2020. https://doi.org/10.1029/2019MS002009

Schwingshackl C, Hirschi M, Seneviratne SI (2017) Quantifying spatiotemporal variations of soil moisture control on surface energy balance and near-surface air temperature. J Clim 30(18):7105–7124. https://doi.org/10.1175/JCLI-D-16-0727.1

Schwingshackl C, Hirschi M, Seneviratne SI (2018) A theoretical approach to assess soil moisture–climate coupling across CMIP5 and GLACE-CMIP5 experiments. Earth Syst Dyn 9(4):1217–1234. https://doi.org/10.5194/esd-9-1217-2018

Seneviratne SI, Lüthi D, Litschi M, Schär C (2006) Land–atmosphere coupling and climate change in Europe. Nature 443(7108):205–209. https://doi.org/10.1038/nature05095

Schaller N, Sillmann J, Anstey J, Fischer EM, Grams CM, Russo S (2018) Influence of blocking on northern European and western Russian heatwaves in large climate model ensembles. Environ Res Lett 13(5):054015. https://doi.org/10.1088/1748-9326/aaba55

Streffing J, Sidorenko D, Semmler T, Zampieri L, Scholz P, Andrés-Martínez M, Koldunov N, Rackow T, Kjellsson J, Goessling H, Athanase M, Wang Q, Hegewald J, Sein DV, Mu L, Fladrich U, Barbi D, Gierz P, Danilov S, Juricke S, Lohmann G, Jung T (2022) AWI-CM3 coupled climate model: description and evaluation experiments for a prototype post-CMIP6 model. Geosci Model Dev 15(16):6399–6427. https://doi.org/10.5194/gmd-15-6399-2022

Sousa PM, Trigo RM, Barriopedro D, Soares PMM, Santos JA (2018) European temperature responses to blocking and ridge regional patterns. Clim Dyn 50(1):457–477. https://doi.org/10.1007/s00382-017-3620-2

Schulz J-P, Vogel G (2020) Improving the processes in the land surface scheme TERRA: bare soil evaporation and skin temperature. Atmosphere 11(5):513. https://doi.org/10.3390/atmos11050513

Seneviratne SI, Zhang X, Adnan M, Badi W, Dereczynski C, Di Luca A, Ghosh S, Iskandar I, Kossin J, Lewis S, Otto FEL, Pinto JG, Satoh M, Vicente-Serrano SM, Wehner M, Zhou B (2021) Weather and climate extreme events in a changing climate. In: Masson-Delmotte, V., Zhai, P., Pirani, A., Connors, S.L., Péan, C., Berger, S., Caud, N., Chen, Y., Goldfarb, L., Gomis, M.I., Huang, M., Leitzell, K., Lonnoy, E., Matthews, J.B.R., Maycock, T.K., Waterfield, T., Yelekci, O., Yu, R., Zhou, B. (eds.) Climate Change 2021: The Physical Science Basis. Contribution of Working Group I to the Sixth Assessment Report of the Intergovernmental Panel on Climate Change, 1513–1766. Cambridge University Press, Cambridge, United Kingdom and New York, NY, USA . https://doi.org/10.1017/9781009157896.013

Tripathy KP, Mishra AK (2023) How Unusual Is the 2022 European Compound Drought and Heatwave Event? Geophys Res Lett 50(15):2023–105453. https://doi.org/10.1029/2023GL105453

Garderen L, Feser F, Shepherd TG (2021) A methodology for attributing the role of climate change in extreme events: a global spectrally nudged storyline. Nat Hazards Earth Syst Sci 21(1):171–186. https://doi.org/10.5194/nhess-21-171-2021

Verdecchia M, Visconti G, Giorgi F, Marinucci MR (1994) Diurnal temperature range for a doubled carbon dioxide concentration experiment: analysis of possible physical mechanisms. Geophys Res Lett 21(14):1527–1530. https://doi.org/10.1029/94GL00188

Woollings T, Drouard M, Sexton DMH, McSweeney CF (2025) Sensitivity of European blocking to physical parameters in a large ensemble climate model experiment. Atmos Sci Lett 26(3):1295. https://doi.org/10.1002/asl.1295

Wehrli K, Hauser M, Seneviratne SI (2020) Storylines of the 2018 Northern Hemisphere heatwave at pre-industrial and higher global warming levels. Earth Syst Dyn 11(4):855–873. https://doi.org/10.5194/esd-11-855-2020

Zhang Y, Boos WR (2023) An upper bound for extreme temperatures over midlatitude land. Proc Natl Acad Sci 120(12):2215278120. https://doi.org/10.1073/pnas.2215278120

Zeppetello LRV, Battisti DS, Baker MB (2019) The origin of soil moisture evaporation "Regimes". J Clim 32(20):6939–6960. https://doi.org/10.1175/JCLI-D-19-0209.1

Zacharias S, Loescher HW, Bogena H, Kiese R, Schrön M, Attinger S, Blume T, Borchardt D, Borg E, Bumberger J, Chwala C, Dietrich P, Fersch B, Frenzel M, Gaillardet J, Groh J, Hajnsek I, Itzerott S, Kunkel R, Kunstmann H, Kunz M, Liebner S, Mirtl M, Montzka C, Musolff A, Pütz T, Rebmann C, Rinke K, Rode M, Sachs T, Samaniego L, Schmid HP, Vogel H-J, Weber U, Wollschläger U, Vereecken H (2024) Fifteen years of integrated terrestrial environmental observatories (TERENO) in Germany: functions, services, and lessons learned. Earth's Future 12(6):2024–004510. https://doi.org/10.1029/2024EF004510

Zängl G, Reinert D, Rípodas P, Baldauf M (2015) The ICON (ICOsahedral Non-hydrostatic) modelling framework of DWD and MPI-M: Description of the non-hydrostatic dynamical core. Q J R Meteorol Soc 141(687):563–579. https://doi.org/10.1002/qj.2378

Zhuo W, Sánchez-Benítez A, Athanase M, Jung T, Yao Y, Goessling HF (2025) Storylines reveal contrasting thermodynamic effects of climate change on 2020/21 East Asian cold extremes. npj Climate and Atmospheric Science 8(1):169. https://doi.org/10.1038/s41612-025-01031-x